5-2014

Infrared Energy Harvesting for Optoplasmonics from Nanostructured Metamaterials

Gregory Thomas Forcherio
University of Arkansas, Fayetteville

Infrared Energy Harvesting for Optoplasmonics from Nanostructured Metamaterials

Infrared Energy Harvesting for Optoplasmonics from Nanostructured Metamaterials

A thesis submitted in partial fulfillment
of the requirements for the degree of
Master of Science in MicroElectronics-Photonics

by

Gregory Thomas Forcherio
Southeast Missouri State University
Bachelor of Science in Engineering Physics and Mathematics, 2012

May 2014
University of Arkansas

This thesis is approved for recommendation to the Graduate Council.

Dr. D. Keith Roper Thesis Director	Dr. Surendra P. Singh Committee Member
Dr. Morgan E. Ware Committee Member	Prof. Kenneth G. Vickers Ex-Officio Member

ABSTRACT

Metamaterials exhibit unique optical resonance characteristics which permit precise engineering of energy pathways within a device. The ability of plasmonic nanostructures to guide electromagnetism offers a platform to reduce global dependence on fossil fuels by harvesting waste heat, which comprises 60% of generated energy around the world. Plasmonic metamaterials were hypothesized to support an exchange of energy between resonance modes, enabling generation of higher energy photons from waste infrared energy. Infrared irradiation of a metamaterial at the Fano coupling lattice resonance was anticipated to re-emit as higher energy visible light at the plasmon resonance. Photonic signals from harvested thermal energy could be used to power wearable medical monitors or off-grid excursions, for example. This thesis developed the design, fabrication, and characterization methods to realize nanostructured metamaterials which permit resonance exchange for infrared energy harvesting applications.

The following signatories attest that all software used in this thesis was legally licensed for use by Mr. Gregory T. Forcherio for research purposes and publication.

Mr. Gregory T. Forcherio Student	Dr. D. Keith Roper Thesis Director

This thesis was submitted to http://www.turnitin.com for plagiarism review by the TurnItIn company's software. The signatories have examined the report on this thesis that was returned by TurnItIn and attest that, in their opinion, the items highlighted by the software are incidental to common usage and are not plagiarized material.

Prof. Kenneth G. Vickers Program Director	Dr. D. Keith Roper Thesis Director

ACKNOWLEDGEMENTS

This thesis signifies the advisement and dedication of those who inspired my scientific pursuits. Foremost, I want to acknowledge my advisor, Dr. Keith Roper for providing me with the opportunity to pursue a graduate degree. His patience and relentless pursuit of scientific innovation have been a great source of inspiration. I only hope that the opportunity to conduct research with someone of a different scientific background has benefitted him the way it has me. It has been a great privilege.

The current and former members of the NanoBio Photonics Lab have been an instrumental resource during my time at the University of Arkansas. In particular, I would like to express my gratitude to Dr. Phillip Blake for more invaluable discussions than I can count, and for showing me the ropes of research from the moment I stepped on campus. I am grateful to my other friends and colleagues in the group for their contributions to my research: namely, Jeremy Dunklin, Drew DeJarnette, Xingfei Wei, Dr. Milana Lisunova, James Proctor, Justin Norman, Caitlyn Chambers, and Carter Bodinger. The guidance and leadership of Prof. Ken Vickers was vital to my professional development during Dr. Roper's tenure at the National Science Foundation. I want to thank my committee members, Drs. Morgan Ware and Surendra Singh, for their support in completion of this work.

Of course, I would not be where I am today without the guidance and training from my former mentors at Southeast Missouri State University and Purdue University. Dr. David K. Probst was a model of professionalism in my young career, and always pushed me into opportunities he knew would benefit my pursuits. I am appreciative of the encouragement from Drs. Jian Peng and Margaret Hill to pursue a graduate degree. Dr. Mark S. Lundstrom provided

me with the opportunity to study photovoltaic technology at Purdue University, for which I am forever indebted. That experience is a key foundation to my studies today.

Lastly, I want to express my most sincere thanks to my parents, Chris and Brenda. They have served as the sole inspiration to pursue my dreams since I was a child, and their support has meant everything to me. I owe my success to my beautiful fiancé, Heather, who has been an unwavering pillar of encouragement and support. My success is their success.

Financial Support. I want to take this opportunity to express my gratitude to the organizations that made this research possible: the National Science Foundation, University of Arkansas Foundation, and the Walton Family Charitable Foundation. Any opinions, findings, and conclusions expressed in this thesis are my own and do not necessarily reflect the views of the National Science Foundation. I am forever grateful to the University of Arkansas for supporting of my academic endeavors by awarding me with the Doctoral Academy Fellowship.

TABLE OF CONTENTS

LIST OF FIGURES

LIST OF TABLES

Chapter 1

THERMAL ENERGY HARVESTING

The development of secure, sustainable energy sources has been a cornerstone of scientific research since the 20th century to reduce global dependence on fossil fuels. These efforts have decreased proportional fossil fuel consumption 10% over the last 50 years with the advancement of nuclear fission, solar photovoltaic, wind turbine, and biofuel technologies.[1] The International Energy Agency has devised a renewable energy policy to save over a projected 160 gigatonnes in carbon dioxide emissions over a 33% energy demand increase by 2035.[1,2] However, history suggests a half-century transition period to fully realize a new energy technology,[3] despite the diminishing economic gap between fossil fuels and renewables. Improving overall efficiency of modern production methods by harvesting thermal energy could help mitigate this transition period and accommodate rising demand without further emissions. Recycling waste heat has long been a goal of the scientific community.[4–6] This chapter discusses the motivation behind this goal, and outlines the objective of research to convert infrared energy into electronic and/or photonic signals.

1.1 Motivation

Approximately 60% of generated energy is lost as dissipated heat.[7,8] Recycling this radiated energy back into the grid or to power complementary, stand-alone devices offers a potential 10 terawatt reduction in global energy demand in an emission-free fashion.[3,8] Net generation efficiency increases from harvesting dissipated heat could help meet demand as the world population draws near 9 billion by 2050,[9] without tapping into fossil fuel reserves or

adding generators. Reduction of carbon dioxide emissions into the atmosphere complements a lower demand for energy production.[1,7] The ability to power stand-alone devices by recycling dissipated heat supports conserving our energy resources, and offers an opportunity to realize battery-free, low-power devices such as wireless sensor networks. The U.S. Department of Energy believes enhancing net output efficiency and decarbonizing energy generation, while lowering power requirements of our devices (i.e. conservation), are essential for a sustainable, prosperous future.[1]

1.2 Market Considerations

Harvesting thermal energy as stand-alone power is a growing market expected to eclipse $60M by 2017[10] with prospects of noise-free, solid-state, sustainable power generation. The biological device, electronic, industrial, and transportation sectors of the economy are primary funders of this market with interest in thermoelectric materials.[7,10] Thermoelectric materials convert a thermal gradient to direct-current electricity using the Peltier-Seebeck effect.[4] The biological and health sector envisions wearable and/or implantable medical monitors. The electronics sector favors thermal energy harvesting as a platform for low-power microchips and devices, as well as smart glass technologies. The industrial sector wants to recover heat from power plant operations, and plans to develop self-powered sensory monitors for buildings/equipment. The transportation sector would like to recycle the 33% of combustion energy which is transduced to exhaust heat.[1,7]

The cost of thermoelectric materials, bismuth telluride for example at over $3/W for a 100 ˚C gradient, has limited thermal harvesting devices to niche markets which can afford high investment capital.[5,7,11] The high cost is primarily attributable to the price of tellurium at

$140/kg. Consideration of venture and technologic risk suggest wearable electronics and remote power generation as two of the most attractive opportunities for research-to-marketplace transition.[7] This is because each of these applications belong to a market willing to invest the necessary capital. The cost of thermoelectric materials has precluded adoption in the automotive industry despite fuel economy gains above 3%.[12,13]

Combining the geometric footprint of electronics with the transmission speed of photonics could support the global push towards low-power devices, while enhancing clockspeeds.[14,15] Though electronic transistor performance improves with scaling according to Moore's Law, the heat generated from geometric confinement has minimized processor speed enhancements in recent years.[14] Optical data interconnects between electronic devices would enable low power operation with higher data transmission rates. Lowering energy requirements of devices which the biological and electronic sectors aim to power with waste heat could make the use of conventional thermoelectrics more economically viable.

1.3 Infrared Harvesting Applications

Modern approaches to harvesting thermal energy for electricity include thermoelectric materials and thermophotovoltaic devices. Research in thermoelectric materials increased upon discovery of bismuth telluride alloys in the 1950s because of their inherently high figure of merit ($ZT \approx 1$).[4] Modern nanostructuring techniques have improved these devices but have not met the figure of merit target, $ZT \geq 3$, to compete with mechanical processes.[4,13] Thus current thermoelectric technology is limited to large area niche applications due to efficiencies below 20% (1000 ˚C source) and the price of tellurium.[4,7,13] Unfortunately, 2/3 of the overall cost is relegated to the balance-of-system and fixed costs,[7] leaving little room for improvement.

Thermophotovoltaics are another approach for converting heat to electricity, where the bandgap of a semiconductor is tailored to match the energy of infrared radiation from an emissive body.[16–18] This avoids losses associated with Joule heating and spectral-mismatches in conventional solar photovoltaics. To date, most research has focused on engineering a separate emitter component to convert solar emission into a narrow-band spectrum.[17–20] Ultimate efficiencies of thermophotovoltaic systems have been reported above 30% at temperatures greater than 700 ºC,[17,18,20] which however requires careful consideration of elemental melting points. Thermoelectric and thermophotovoltaic devices are considered as options for off-setting alternator loads in vehicles, power generation for remote military excursions, and heat recovery from power plant operations.

Wearable electronics, such as *in situ* medical monitoring, may be possible using energy harvested from body heat.[21] Body heat can provide around 8 mW/cm^2 of power at the skin surface. Bismuth telluride thermoelectrics can transduce body heat to about 20 $\mu W/cm^2$, which is enough to power a quartz watch or wireless sensor module.[11,21,22] However operating voltage for these electronic devices requires > 10^3 bismuth telluride junctions, whose cost favors use of conventional batteries.[11] Development of these, and similar, devices with next-generation optical interconnects and logic may lower operation energy requirements. The military has funded research into body heat-harvested personal area networks and medical monitoring, aiming for health and psychological sensors of soldiers in harsh climates.[23,24]

Complementing conventional silicon-based electronics with optical interconnects to reduce device power requirements may represent the next-generation of logic devices.[14,15,25] Interconnects in microprocessors compromise nearly 80% of total power consumption.[25] Optical transmission avoids resistive losses at 1000-fold higher data densities, while offering additional

processing capabilities such as wavelength-division multiplexing.[14,25] However, lack of efficient visible to near-infrared emission from bulk silicon and the size of optic-electronic transition components has precluded combination of electronic and photonic devices.[14,25,26] Nanoscopic structures have been lithographed onto silicon CMOS for tunable emission between 400 nm and 700 nm.[27–30] However the required 30 keV electron beam presents additional integration and power issues.[29] A similar vision where nanoscopic structures function as a photon source could be possible using the same heat dissipation which has prevented processor clock-speed advances for a number of years. This vision could enable facile integration of photonic interconnects, while opening opportunities for all-optical logic circuits.[14,15,31,32]

Heat is dissipated from a body as infrared electromagnetic radiation. Each aforementioned application functions using visible through near-infrared wavelengths. Solid-state conversion between these two electromagnetic spectra may provide an adoptable platform for these technologies. Remote power generation could be amenable to conventional mid-bandgap semiconductors using thermophotovoltaic principles. Photonic interconnects for enhanced data transmission could be adopted by fiber-coupling visible photons generated via heat dissipation from adjacent electronic components. Self-powered devices, such as wearable medical diagnostics, could be realized by coupling thermophotovoltaic electric generation with low-power electronic-photonic logic circuits, or ultimately all-optical device operation.

1.4 Research Objective

The objective of this research is to harvest radiated infrared energy using artificial materials with an optical resonance characteristic to allow an exchange of energy between two distinct frequencies. For example, infrared energy could be manipulated into visible light using a

nanostructured metamaterial for use in a compatible device. Figure 1.1 shows the critical research steps which comprise this study. This thesis will focus on the development and identification of design considerations, fabrication techniques, and characterization methods of nanostructured metamaterials for infrared energy harvesting.

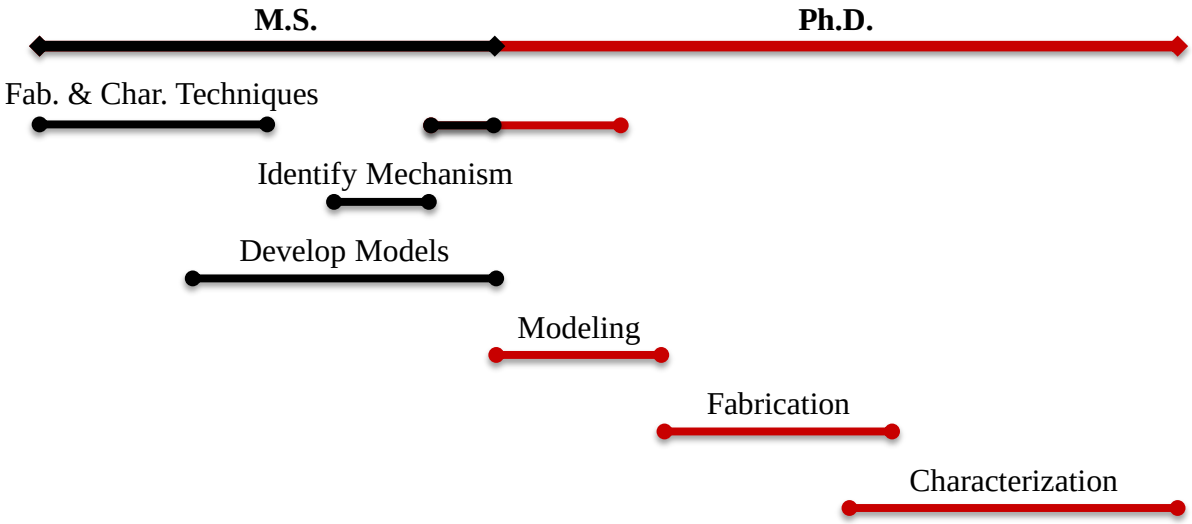

Figure 1.1: Gantt chart timeline of research objectives.

Chapter 2

NANOSTRUCTURED METAMATERIALS

Plasmonic metamaterials are engineered, artificial media not found in nature, with unique optical properties which permit nanoscale energy manipulation. These properties arise from the ability of noble-metal nanoparticles to support surface plasmons, coherent electron oscillations, in response to resonant electromagnetic energy. Periodic ordering of nanoparticles introduces diffractive modes, which can alter plasmon resonance favorable for modal energy exchanges. Ring structures exhibit intense, highly tunable plasmon resonances favorable for wavelength-specific applications. This chapter outlines modeling techniques to guide design of metamaterials and examines structure and lattice constant influences on the electromagnetic response of nanoring lattices.

2.1 Plasmon Resonance

Subwavelength, metallic structures allow manipulation of electromagnetic energy through their ability to support plasmons.[31] The geometric and physical configuration of these nanostructures determines energy, intensity, and breadth of optical absorption and scattering behavior in response to incident electromagnetism. Resonant electromagnetic energy will stimulate a surface plasmon- a quasi-particle of coherent electron gas oscillations confined to a metal-dielectric interface.[33,34] Plasmons geometrically confined along the surface of a nanostructure are referred to as localized surface plasmons. The localized surface plasmon resonance (LSPR) is dependent on size,[35,36] shape,[33,35,37,38] and composition of a nanostructure. A dipole LSPR on two gold spheres is shown in Figure 2.1.

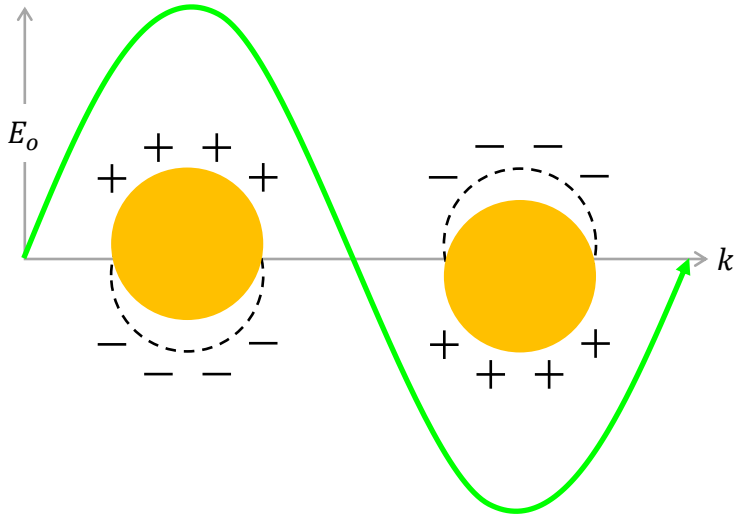

Figure 2.1: Induced dipolar plasmon on a subwavelength, gold sphere. E_o is the electric field amplitude and k is the wave vector.

The absorptive behavior of plasmonic structures, via energy transfer between photons and electron gas, allows localization of light resulting in intense electric near-fields. Plasmonic absorption is the basis of surface-enhanced Raman spectroscopy[39] and heating[40–42] applications. Intense electric fields at the nanostructure surface are of interest in thin-film photovoltaics to enhance charge carrier separation at semiconductor junctions, and to increase spectral absorption at desired wavelengths.[31,43] LSPR is additionally dependent on the local dielectric environment to which the plasmons are confined at the nanostructure surface, causing spectral shifts as the basis for refractive index sensors.[44–46] These examples are representative of opto-electronic applications for which plasmonic devices have been considered. This thesis considers utilization of plasmons for harvesting waste radiative energy.

2.2 Diffractive Coupling in Nanoparticle Lattices

Periodic configuration of nanostructures into lattices at spacings near or above the LSPR wavelength permits Fano resonant coupling between near-field resonance and far-field

diffraction modes.[47–50] This coupling arises from in-phase constructive interference between scattering nanoelements within the lattice, thus enhancing the net electromagnetic field incident to each nanostructure. Therefore, irradiation of periodically arrayed nanostructures results in two primary spectral features: the plasmon resonance (PR) and lattice resonance (LR). Diffractive coupling Fano resonances were first reported in 2005 for nanosphere lattices,[50] demonstrating a narrow, intense extinction peak near the lattice constant at a lower energy than the PR. To date, simple structures such as spheres and discs have been considered in Fano resonant lattices due to fabrication considerations[50–52] and computational availability of analytical polarizability.[48,49] Diffractive coupling is primarily influenced by the lattice constant, d, and polarization of the incident electromagnetic wave.[48]

The most common two-dimensional periodic configurations considered in the literature

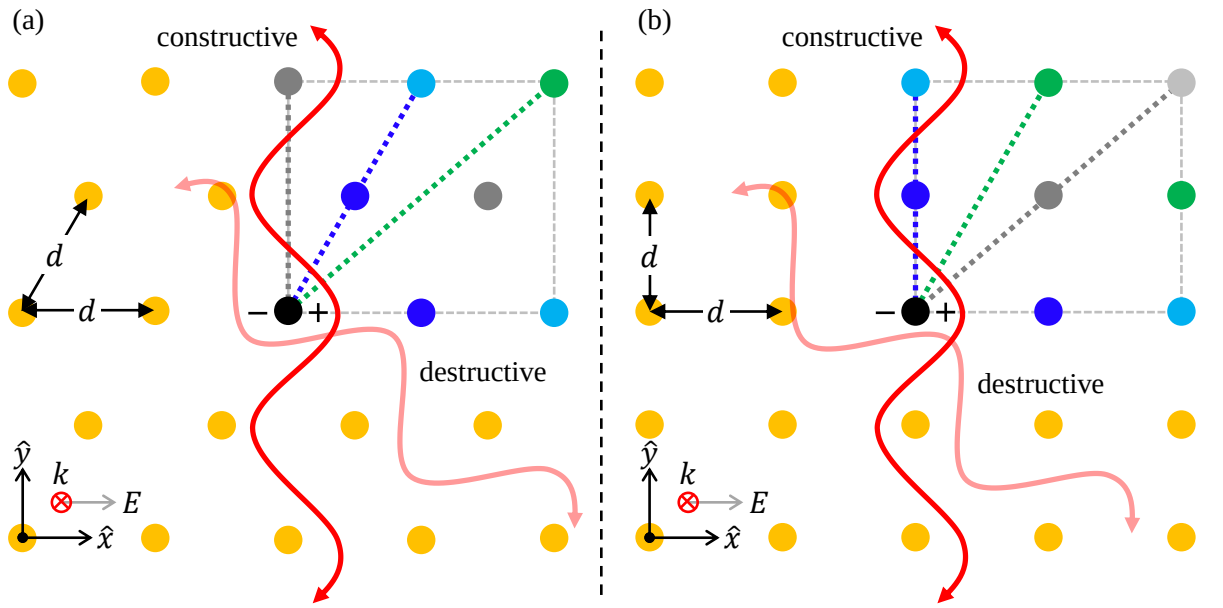

Figure 2.2: Schematic representations of (a) hexagonal and (b) square arrayed elements (circles) with lattice constant d under normal optical incidence with $\hat{x}$ polarization. Grid in upper quadrant of each lattice color coordinates diffractive scattering modes relative to the black center element. Elements which support diffraction at the lattice constant (blue), primary diagonal (gray), and off-axis positions (green) are colored within this quadrant. Complementary spaced elements within each mode chain are colored lighter.

are rectilinear and hexagonal lattices. A rectilinear lattice consists of nanoelement chains of vertical and horizontal spacing (d_y and d_x, respectively) in cardinal directions. Square lattices ($d_y = d_x$) are a special consideration of rectilinear configuration which exhibit $\pi/2$ rotational symmetry for an isotropic response to $\hat{x}$ and $\hat{y}$ polarization. Hexagonal lattices exhibit $\pi/6$ rotational symmetry by arranging nanoelements at the vertices of a hexagon centered around an element. The configurations of these lattices are illustrated in Figure 2.2.

Fano resonance from coupling between LSPR of nanospheres and diffractive modes of square and hexagonal lattices was observed in Figure 2.3. These spectra illustrated a fundamental difference in optical response between the two lattice types at a common lattice constant due to polarization dependence. The PR in each spectra was dissimilar because different sphere diameters (140 nm for hexagonal and 180 nm for square), and therefore different LSPR, were used for each lattice to provide high intensity LR peaks. These parameters were chosen according to previous work which facilitated their specification to provide high spectral extinction performance in square and hexagonal arrangements.[49,53] Square lattices generally

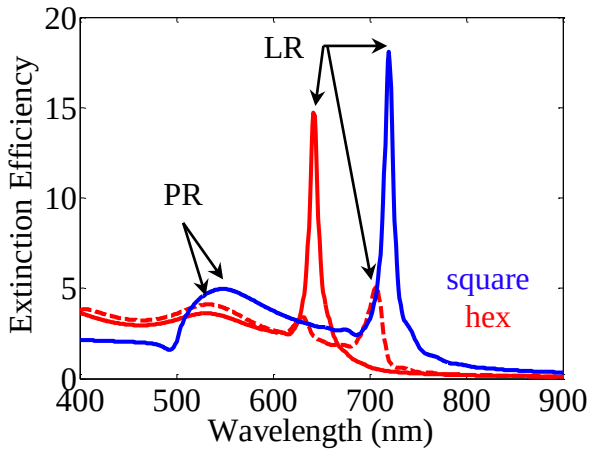

Figure 2.3: Spectral extinction for a square (blue) and hexagonal (red) lattice of 180 nm and 140 nm diameter gold nanospheres, respectively, at a lattice constant of 700 nm using the finite coupled dipole approximation (30 x 30 lattice). Two spectra are shown for the hexagonal lattice, corresponding to $\hat{x}$ (solid) and $\hat{y}$ (dotted) polarizations to elicit different diffraction modes.

exhibit more intense LR peaks.[53] LR peaks exhibited by hexagonal lattices may be tuned according to incident polarization, though highest intensities were observed at half-wavelengths of the $d\sqrt{3}$ spacing (gray mode in Figure 2.2). It should be noted that different structures/shapes may exhibit slightly different optical responses (intensities, peak shape, etc.), though Fano coupling trends between LSPR and diffractive modes were anticipated to be consistent.

2.3 Approximate Dipole Modeling of Metamaterials

The optical behavior of nanostructured metamaterials can be numerically modeled using approximate dipolar solutions to Maxwell's equations. Two such models include the discrete dipole (DDA) and coupled dipole approximations (CDA). These models reduce computational time and target generation over higher order models such as boundary (BEM) and finite element models (FEM) and finite difference time domain (FDTD),[54] whose solutions result from a discretization of time and space. Approximate dipole methods describe arbitrary assemblies of nanoparticles as polarizable electromagnetic dipoles, which is valid for structures which exhibit dipolar and/or quadrupolar behavior.[48] This section overviews the use of the DDA and CDA in evaluating the response of nanostructured metamaterials to optical stimulation.

2.3.1 Discrete Dipole Approximation

The DDA solves Maxwell's equations for arbitrary target geometries by approximating the geometry as an array of dipolar points, resulting in the absorption and scattering of incident electromagnetic waves.[55,56] Target geometries are generated as a defined continuous structure discretized into a cubic array of dipoles, each with a polarizability chosen according to a Lattice Dispersion Relation.[57] Distribution of these discretized geometries into lattices results in diffractive scattering, for which DDA calculates the scattering amplitude and Mueller matrices.[58]

Coupling of these solutions is performed to give far-field absorption and scattering efficiency. Approximation of the induced nanostructure polarization (P) allows the DDA to calculate the electromagnetic response (E) of its constituent polarizable (α) dipoles according to:[59]

$$P = \alpha E \tag{2.1}$$

Accuracy of DDA models relies on the target discretization, most prominently the number of dipoles. Previous work in analyzing influence of geometry discretization on spectral results by Blake showed that targets with dipole counts on the order of 10^3-10^4 are suitable.[60] Targets with less dipole counts tend to exhibit a blue-shifted LSPR and PR (single particle versus lattice), though trends between the PR and LR features are consistent with higher count targets. Blake developed a Matlab program to discretize geometries,[60] which was aimed to cylinders, discs, and more complex ring shapes by implementing a Bresenham algorithm.[61] An example of a discretized disc is shown in Figure 2.4. DDA models are computationally intensive due to the required number of dipoles for solution convergence. Therefore, simulations were performed on the 12- or 16-core node Razor clusters with at least 24 GB of memory, at the Arkansas High Performance Computing Center.

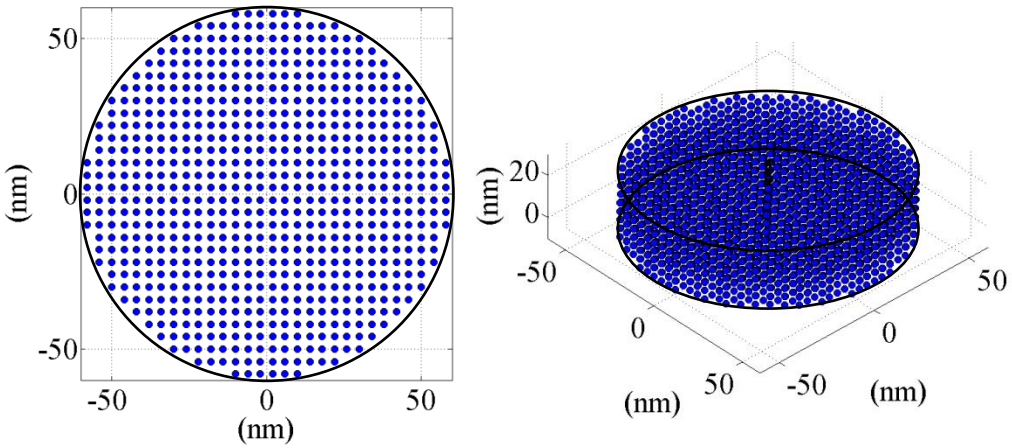

Figure 2.4: Discretized disc with 5150 dipoles according to a 4 nm inter-dipole spacing. Disc is 60 nm in radius and 20 nm in height. The non-discretized disc can be visualized by black lines.

2.3.2 Coupled Dipole Approximation

The CDA solves Maxwell's equations for nanostructure lattices by treating each nanoelement within the lattice as a scattering, polarizable point dipole.[45,52] Scattering contributions from neighboring elements within a particular chain (expressed as modes in Figure 2.2) are used in calculation of the retarded dipole sum. Far-field diffraction dominates the retarded dipole sum when wavelength is approximately the inter-particle spacing of the chain.[45]

A rapid semi-analytical solution to the CDA (rsa-CDA) developed by DeJarnette, Norman, Taylor, Harbin, and Roper reduces net computational time by exploiting the rotational symmetry of periodic lattices to reduce function calls.[45,48,49,62] Work by DeJarnette allowed quadrupole polarizability to be considered in CDA models, resulting in better agreement with higher order models.[48] However, implementations of the CDA were constrained to nanostructure shapes whose polarizability scalar could be analytically described, e.g. spheres.

2.3.3 Polarizability Extraction

The DDA and CDA were used together to evaluate lattices of complex nanostructures by extracting the polarizability calculated by DDA, and using the CDA to extend that polarizable geometry into a lattice.[63] This allowed rapid optimization of the lattice constant to evaluate diffractive enhanced spectral features in lattices of arbitrary structures. The DDA automatically calculates an effective polarizability for the discretized structure based on the polarizabilities of its constituent dipoles according to:

$$\alpha_{eff} = \sum_{j=1}^{n} \frac{{d_{di}}^3 P_j}{E_{in}} \tag{2.2}$$

where d_{di} is the inter-dipole spacing, P_j is the complex polarization of the jth dipole per unit volume, and E_{in} is the incident complex electric field. However the DDA did not readily output

the calculated effective polarizability function, so code modifications allowed a file containing the values to be used in the CDA. The DDA can model the same lattices, but computational requirements are favorable for the CDA to simulate effects of diffraction.

Use of the rsa-CDA to evaluate nanostructured metamaterials from DDA-extracted polarizability functions was observed to reduce computation time 40,000-fold with less than 1% error in peak locations over full DDA models.[63] Ring structures were used in evaluation of this approach, though it is anticipated to be amenable to other arbitrary shapes (e.g. pyramids, stars, etc.) provided that predominately dipolar behavior is exhibited. Drawbacks to this approach included the variation of simulated extinction efficiency magnitude across different shapes due to the dependence on cross sectional area in the plane of incidence. The CDA calculates extinction efficiency according to the cross sectional area of a sphere, the shape for which the algorithm was developed. Therefore the input particle radius for the CDA (determined by equalizing cross sectional area of shape in question to that of a circle) can be increased/decreased to match magnitude calculated by the DDA.[63] However this was anticipated to effect calculation of the absorption and scattering components of extinction in the CDA. Instead spectra were multiplied by a constant (DDA magnitude divided by CDA magnitude evaluated at the highest peak) to circumvent this issue.[64] Comparison of extracted polarizability results from this technique with results from analytical polarizability models of other structures is subject of ongoing work in the NanoBio Photonics Lab.

2.4 Nanoring Metamaterials

Rings exhibit intense, highly tunable plasmonic resonances in the near infrared spectrum. These advantages over other polygons of equal volume such as spheres, cubes, and other

polyhedra arise due to their multiple geometric parameters and relatively high surface area to volume ratio.[60,65] Resonance behavior of nanorings may be enhanced by diffractive modes when ordered into lattices. Evaluation of inter-related effects of ring structure and spacing on their infrared behavior is of interest to infrared applications, owing to the lower amount of energy required to excite plasmons.

A rectilinear lattice of rings can be described by the following geometric parameters: inner radius (r_{in}), wall thickness (t), height (h), and lattice constant (d_x and d_y). Figure 2.5 illustrates these parameters. Section 2.4.1 highlights influence of inner radius and wall thickness on the LSPR wavelength, intensity, breadth, and relative absorption to scattering ratio of single rings using the DDA. Effects of height were not explicitly considered because previous work indicated that the LSPR of rings is primarily influenced by their aspect ratio, (t/r).[65] Effective polarizability was extracted for an optimal ring geometry to examine the influence of lattice

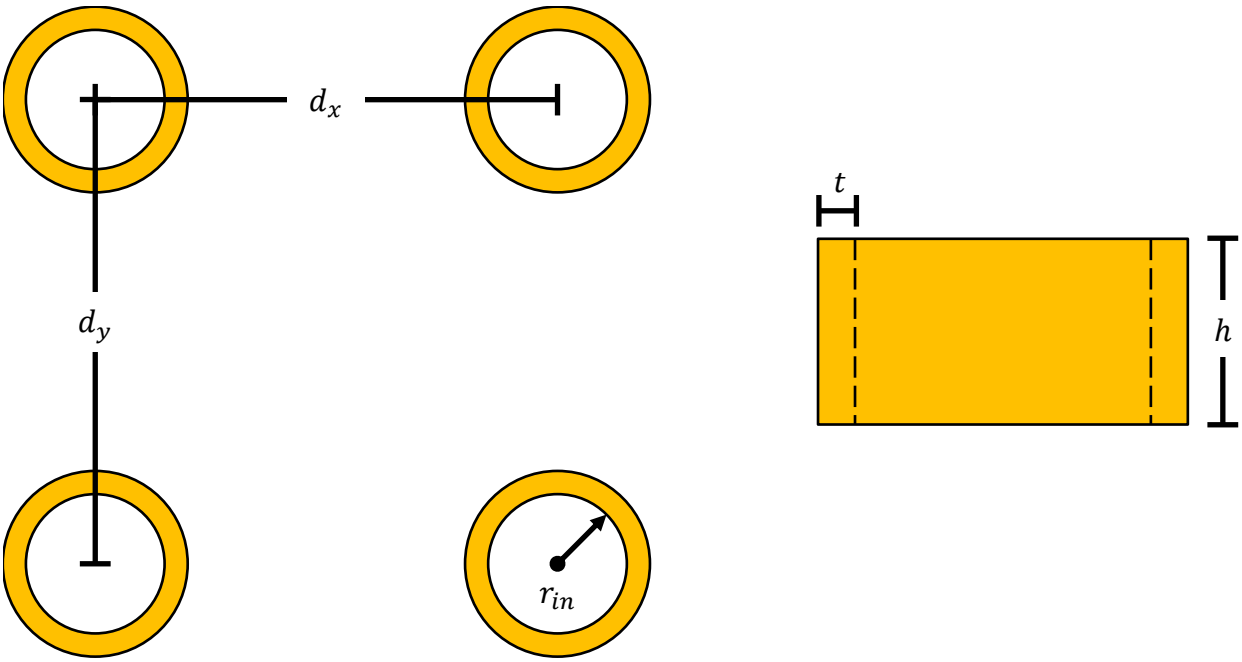

Figure 2.5: Geometric parameters for a square unit lattice of rings: r_{in} is the inner radius, t is the wall thickness, h is the ring height, and d_x and d_y are the lattice constants in the x and y directions, respectively. Adapted from Ref. 60.

constant in square lattices ($d = d_x = d_y$) to determine diffractive enhancements on plasmonic behavior using the rsa-CDA.

2.4.1 Single Rings

Plasmonic behavior of a nanoring is tunable by varying its radius and wall thickness. Charge distribution on the walls of the ring can give two dipolar plasmon modes at specific geometries,[65–67] commonly denoted as low-energy bonding and high-energy anti-bonding.[68] Bonding is where all positive charge and all negative charge appear on their respective opposite sides. Anti-bonding is when a dipole appears on adjacent walls. The observations and trends discussed herein focus on the bonding mode due to its tunability and increased light extinctions.

Optical extinction spectra for nanorings with r_{in} between 20 nm to 100 nm at t = 10 nm and 20 nm are shown in Figure 2.6. LSPR peak shapes appeared largely Lorenztian, though some peaks exhibited asymmetry due to interactions between the inner and outer walls.[64] LSPR wavelengths in the near infrared spectrum were observed from about 650 nm to 1150 nm. LSPR wavelengths reported in the literature range from 800 nm to 1400 nm for nanorings with inner

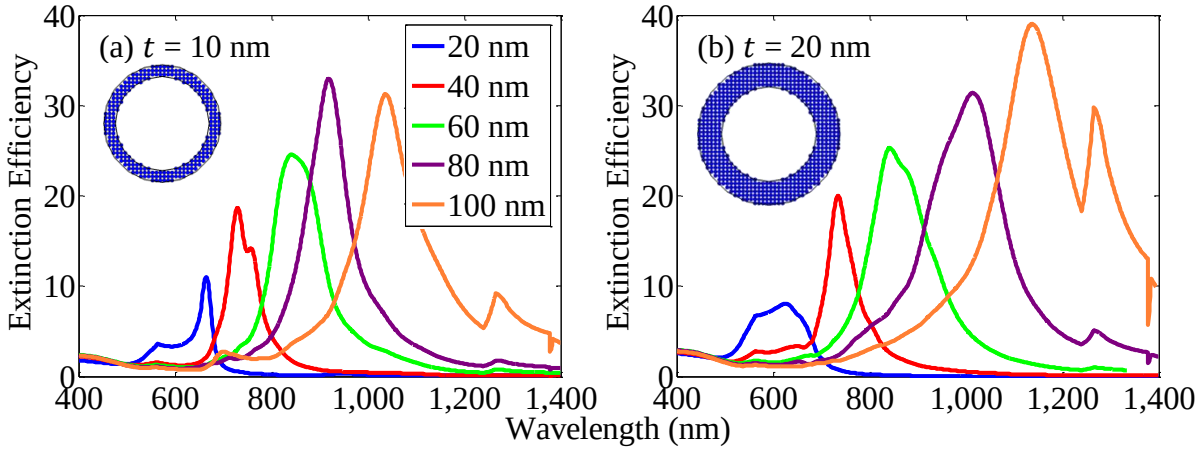

Figure 2.6: Optical extinction spectra of single nanorings with r_{in} = 20 nm (blue), 40 nm (red), 60 nm (green), 80 nm (purple), and 100 nm (orange) at t = (a) 10 nm and (b) 20 nm with h = 50 nm. Features at 564 nm, 1265 nm, and 1378 nm are artifacts of the refractive index data used, not plasmonic activity from varying nanoring geometry. Adapted from Ref. 64.

radii of 45-50 nm at 10-20 nm wall thickness.[65,69–71] Peak locations and shape in Figure 2.6 compared favorably with simulated (FDTD) and experimental data from Huang *et al*.[71]

Increasing the inner radius of nanorings red-shifted and broadened the LSPR, as shown in Figure 2.7.[64] The LSPR red-shift was attributable to phase retardation across the structure due to interactions between different oscillation modes (dipole, quadrupole, etc.).[36] Nanospheres exhibit a similar LSPR red-shift for radius increases. Plasmon red-shifts have been experimentally observed when increasing r_{in} from 50 nm to 105 nm.[71] Broadening of the LSPR (Figure 2.7(b)) could have been attributable to phase retardation across the structure as well, which occurs in spheres.[36] Rings behaved analogously to spheres in this regard because coupling between the inner and outer walls of a ring is similar to inter-shell coupling in a hollow sphere.[65]

Adjusting wall thickness tuned the LSPR wavelength and influenced the absorptive behavior of nanorings.[64] The influence of wall thickness on LSPR was dependent on the radius, as observed in Figure 2.8(a). Blue-shifting with increasing t was observed for small inner radii ($\lesssim$ 40 nm), which was consistent with Drude-like dielectric functions employing an electrostatic

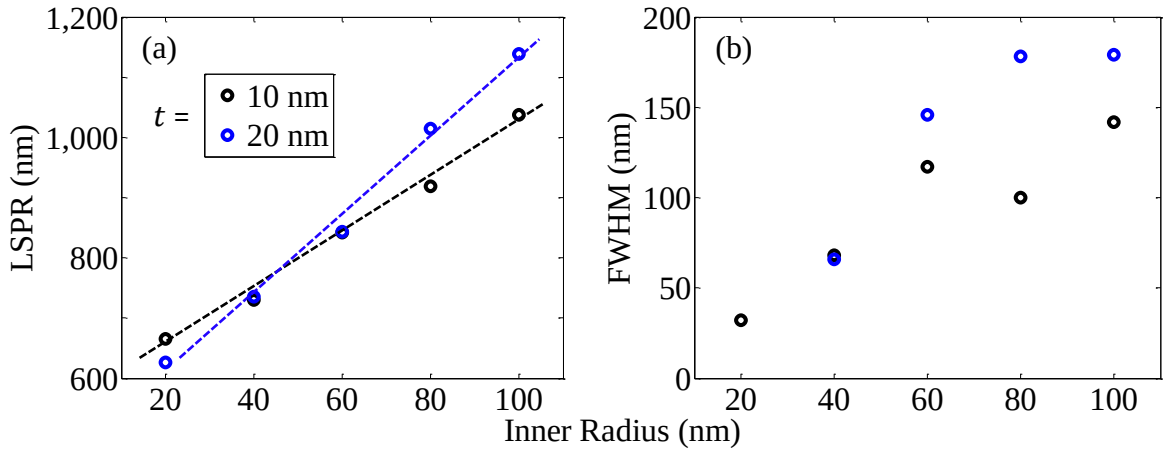

Figure 2.7: Influence of the inner radius of a nanoring on the LSPR (a) wavelength and (b) breadth. Ring thicknesses of 10 nm (black) and 20 nm (blue) are shown. The FWHM of r_{in} = 20 nm at t = 20 nm was withheld from (b) to avoid skewing perceived trends, due to an anomaly arising from refractive index artifacts.

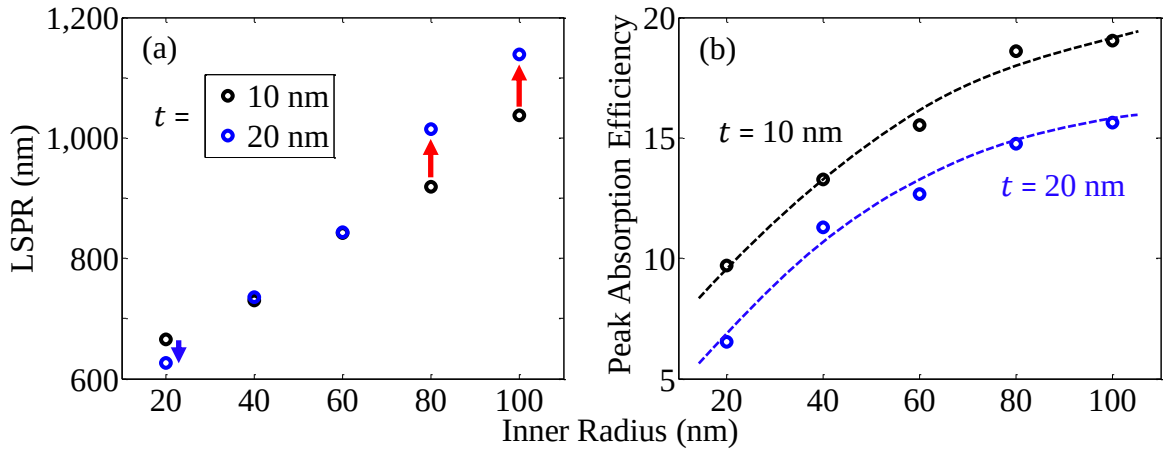

Figure 2.8: Influence of nanoring wall thickness on LSPR. Graph (a) shows LSPR wavelength as a function of r_{in}, with arrows highlighting peak shift after increasing t from 10 nm (black) to 20 nm (blue). Red and blue colored arrows correspond to red- and blue-shifts, respectively. Graph (b) shows absorption efficiency magnitude as a function of r_{in} at 10 nm and 20 nm thicknesses.

assumption and experimental data of rings with small inner radii.[65,71,72] However, larger ring dimensions did not follow this same blue-shifting trend. At higher inner radii, an LSPR red-shift (≥ 80 nm inner radius), broadening (≥ 60 nm inner radius), and extinction magnitude increase (100 nm inner radius) was observed. Available analytic methods for predicting LSPR in rings were limited to the quasi-static case, which might not have been valid for these larger rings. It appeared that radius began to dominate the aspect ratio in these cases, which made variance in wall thickness less important. Figure 2.8(b) shows thinner rings exhibited 18-48% higher absorption, despite generally higher extinction magnitudes for thicker rings.

A nanoring with r_{in} = 80 nm and t = 10 nm was observed to exhibit the highest cumulative absorption and extinction potential among the considered geometries.[64] High plasmonic absorption is desired for applications which requiring intense electric near-fields, such as heating. However adequate scattering behavior is required to support lattice diffraction enhancements to plasmonic activity. Balance between extinction and absorption meets needs of many optoplasmonic applications, in addition to the objective of this thesis.

2.4.2 Fano Resonant Nanoring Lattices

Periodic ordering of nanorings (of geometry identified in § 2.4.1) resulted in Fano resonant coupling when the lattice constant, d, was near or above the single-particle LSPR wavelength.[64] Figure 2.9 shows extinction spectra of such nanoring lattices (solid lines), and the single-particle (dotted line) spectra for comparison. LR features were observed for lattices with $d \geq 900$ nm, near the single-particle LSPR of 919 nm. Lattices with lattice constants near or greater than this wavelength exhibited a PR feature blue-shifted from the single-particle LSPR, which decreased back to the single-particle LSPR as d increased. LR features appeared generally smaller in magnitude than the PR features in the cases examined. Fano resonance was not observed for lattice constants lower than 900 nm which red-shifted the PR, despite occurrence of a diffractive feature corresponding to the cardinal mode illustrated in Figure 2.2.

The PR and LR features monotonically increased in wavelength location as the lattice constant was tuned around the single-particle LSPR.[64] Figure 2.10(a) shows resonance

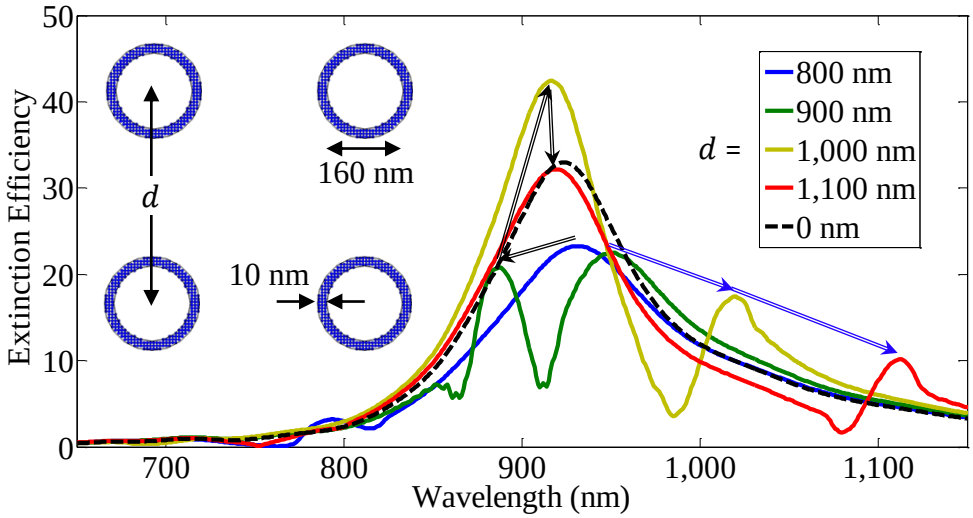

Figure 2.9: Optical extinction spectra for nanoring of r_{in} = 80 nm, t = 10 nm, and h = 50 nm (solid purple) configured into square lattices at spacings, d, of 0 nm (dotted), 800 nm (blue), 900 nm (green), 1000 nm (yellow), and 1100 nm (red). Arrows track PR (black) and LR (blue) features as a function of d. Adapted from Ref. 64.

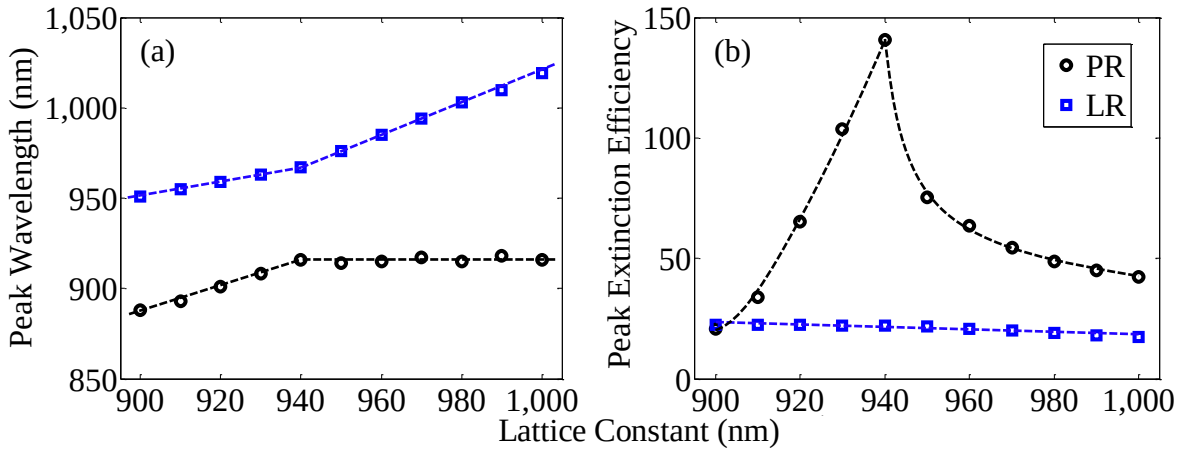

Figure 2.10: PR (black) and LR (blue) (a) peak wavelengths and (b) extinction magnitude as a function of d from 900 nm to 1000 nm with a 10 nm step size. This range was chosen according to the single-particle LSPR at 919 nm. Adapted from Ref. 64.

wavelengths for lattices with d tuned near the single-particle LSPR in 10 nm increments. Increasing the lattice constant consistently increased the PR (black) and LR (blue) wavelengths. It was interesting that each peak appeared to shift linearly with lattice constant, with the two peaks appearing to switch behavior at a common inflection point of 940 nm. Between 900 nm and 940 nm lattice constants, the PR shifted almost twice as much as the LR. However beyond 940 nm, the LR experienced greater shifts while the PR maintained the single-particle location.

Conversely, PR extinction magnitude changed non-monotonically across the same range of lattice constants, also appearing related to this 940 nm inflection point.[64] This is shown in Figure 2.10(b). PR magnitude (black) increased sharply until the lattice constant of 940 nm, where it attained its highest magnitude among the cases considered; a 4-fold increase over the single-particle LSPR magnitude.[64] Larger lattice constants resulted in an exponential-like decay in PR extinction magnitude. Meanwhile, magnitude of the LR feature monotonically decreased across the entire lattice constant range examined.

Configuration of nanorings into square lattices enhanced plasmonic activity upon consideration of the complex polarizability of the ring geometry.[64] For an optimum ring

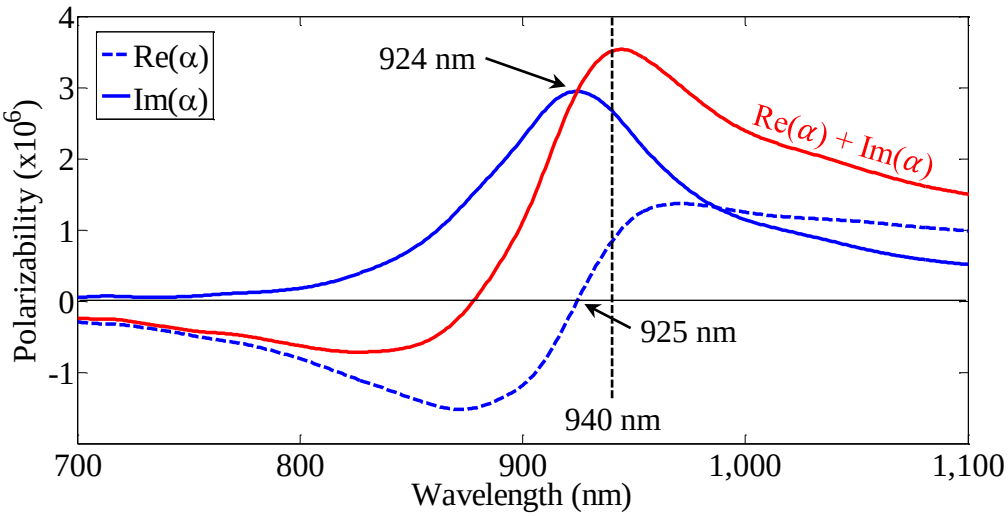

Figure 2.11: Real (dotted blue) and imaginary (solid blue) components of polarizability a nanoring with r_{in} = 80 nm, t = 10 nm, h = 50 nm. The sum of respective Re(α) and Im(α) (solid red) is superposed.

geometry (identified in § 2.4.1), periodic spacing at 940 nm resulted in a PR with 4-fold greater extinction that the single-particle LSPR.[64] The single-particle polarizability of this geometry is shown in Figure 2.11 in blue. Unfortunately the exact relationship between polarizability and these resonance features was unclear, as this intriguing result occurred at a lattice constant not directly explained by any maxima obtained from manipulation of the polarizability function.[64] Maximum of Im(α) did not support this 940 nm lattice constant due to the complementary negative Re(α) at that wavelength,[64] which lent destructive interference to neighboring dipoles.[49] Approximation of the scattering cross section as a spherical particle described by Mie[73] did not fully explain the results, nor did the product of Re(α) and Im(α). Interestingly, summation of respective Re(α) and Im(α) yielded a maximum value at 944 nm, close to the observed optimal lattice constant of 940 nm.[64] Further examination of inter-relating components of polarizability is needed to pinpoint the influential factor in determining lattice constants which provide extinction enhancements.

2.5 Summary

The spectral response of nanostructured metamaterials, in particular rings and spheres, were examined using the CDA and DDA models. This technique was anticipated to be amenable to other arbitrary structures. The influence of nanoring structure on the LSPR wavelength, intensity, and bandwidth was examined using the DDA. Increasing nanoring inner radius generally increased LSPR wavelength, breadth, and extinction. Widening the wall thickness tuned the LSPR wavelength and decreased absorption relative to scattering. Extraction of single-particle polarizability from the DDA enabled rapid evaluation of resonance features exhibited by lattices of nanorings using the CDA. Fano resonance between LSPR and diffraction in nanoring lattices primarily affected the extinction amplitude of the PR, whereas LR extinction amplitude remained near or smaller than the PR over a 300 nm range of lattice spacings past the single-particle LSPR. Adjustment of the lattice constant in a nanoring lattice resulted in PR with 4-fold enhanced extinction magnitude relative to the LSPR. This was attributable to cumulative interactions between components of particle polarizability. These modeling techniques and simulations provided a foundation for the rational design of nanostructure lattices for visible and near-infrared applications.

Chapter 3

RESONANCE EXCHANGE MECHANISMS

Metamaterials comprised of periodic subwavelength structures have the ability to engineer the behavior of electromagnetic energy. Plasmon resonances of these structures transduce electromagnetism into dissipated phonons or reradiated photons. Irradiation of lattices comprised of these structures at the lattice resonance may allow an additional pathway to permit an exchange of energy between two resonance modes under the proper conditions. The ability to convert low energy electromagnetism (e.g. infrared) into higher energy electromagnetism (e.g. visible) is a key example of such modal exchange. Both classical and non-classical mechanisms, such as Kirchhoff's Law and frequency doubling for example, have been used to control electromagnetic characteristics of artificial materials for variety of specific opto-electronic applications. This chapter outlines the use of such concepts in developing metamaterials to allow an opportunity for exchange of electromagnetic energy between multiple resonance modes.

3.1 Plasmon-Enhanced Transmission

An exchange of energy between distinct modes within a metamaterial was first observed in plasmonically enhanced transmission through subwavelength apertures.[74] First published in 1998, the Ebbesen research group noticed unusual transmission behavior in experimental spectra of nanoholes drilled into noble-metal thin films which could not be explained by conventional aperture theory.[75] According to theory written by Bethe,[76] transmission spectra of subwavelength holes is proportional to $(d/\lambda)^4$, where d is hole diameter and λ is wavelength, because of the exponential-like decay of the wave's electric field inside the aperture. However

surface plasmons on the front/back surfaces of a film containing such holes compensate for this exponential decay with their respective intense electric fields surrounding the hole.[77] Thus, enhancements over Bethe's theory were realized.[74,78,79]

Exchange of energy between surface plasmons and evanescent photons within an aperture has been subject of much research by expanding experiments to patterned features concentrating light into a single aperture[78] or apertures lattices.[77,80] It appears transmission enhancements in lattices are directly related to the lattice constant and independent of aperture dimension,[78,80] indicating that surface plasmon polaritons (SPP) may be responsible for their optical behavior.[77] SPPs are plasmons which propagate along a metal-dielectric interface. While relationships between metamaterial parameters and transmission enhancements have been well studied, the exact mechanism is still not known. Despite varying theories,[81] it is unanimously agreed that surface plasmons are solely responsible for the energy exchange causing the observed enhancements.[78,79,82]

Babinet's principle says that an electromagnetic correspondence exists between complementary media,[83–85] including plasmonic media.[86,87] For example, a lattice of apertures within a noble-metal film is complementary to a lattice of noble-metal structures in a vacuum, provided the apertures and complementary structures are of the same dimensions.[84,85] Therefore, enhanced transmission observed in aperture lattices arising from SPPs propagation between apertures may have particle lattice equivalence in diffractive scattering. While SPPs assist decaying wave propagation through an aperture, enhanced electromagnetic fields in nanoparticle lattices from diffraction may assist plasmons at the lattice resonance (LR) shift to another resonance mode. Existence of modal energy exchange between SPPs and evanescent photons in aperture lattices suggests modal energy exchange is possible in nanoparticle lattices.

3.2 Kirchhoff's Law of Thermal Radiation

Design of nanostructured metamaterials as emissive media may be guided through Kirchhoff's Law of Thermal Radiation. According to this law, the emissivity of a media is equal to that of its absorptivity.[16,17,88] The absorptive behavior of plasmonic metamaterials can be engineered, and therefore their emissive characteristics may be controlled. Emissivity of a body is defined as the emitted power relative to that of a perfect black body at the same temperature.[88] Higher temperatures yield greater photon densities, as described by the Stefan-Boltzmann Law which states emitted power density is directly proportional to T^4, where T is temperature. As an example, thermophotovoltaic devices have exploited this relationship to provide immense photon densities (generally greater than 1000 ºC) for power generation.[16,17]

Metamaterials with engineered absorptive characteristics have experimentally exhibited corresponding emissive behavior, matching theory with experiments.[16] This supports the use of Kirchhoff's Law in guiding the design and fabrication of metamaterials as photonically emissive media. However work to date has been performed in the low- to mid-infrared wavelengths at high temperatures where high photon densities can be observed. The same principle is applicable to any media desired to support visible wavelength emission, though power densities may be unobservable with conventional detectors. Certain applications may demand high densities (e.g. photovoltaics), and others it may be negligible, such as photonic circuitry.

3.3 Nonlinear Plasmonic Emission

3.3.1 Second Harmonic Generation

Second harmonic generation (SHG) is a process in which two photons at a particular frequency interact with a nonlinear, non-centrosymmetric media and effectively combine to

create a photon at twice the frequency. These frequencies are generally referred to as the fundamental and harmonic frequencies, respectively. This nonlinear optical process was first studied in the early 1960s, when Franken *et al.* experimentally observed SHG in quartz and Bloembergen *et al.* described the electrodynamics of the observed process.[89,90]

Studies of SHG in nanoparticle lattices, with the pump (i.e. incident) wavelength equal to the localized surface plasmon resonance (LSPR), have been of recent interest with the maturation and availability of lithographic technologies. Optical absorption of the nanoparticle lattice at the fundamental frequency has been attributed as the primary factor in SHG efficiency.[91–93] This was illustrated by McMahon *et al*. after matching the LSPR to the fundamental frequency resulted in greater than 10^2 enhancement in SHG signal.[94,95] Rough, non-centrosymmetric nanoparticle morphologies are considered vital for SHG to occur.[91,92,96] However, a reduction in cylinder centrosymmetry with simultaneous particle roughness reduction has been reported to enhance SHG 40-fold,[93] which supports other findings.[97] Higher order oscillation modes can emit at the harmonic frequency,[92,96] with one research group reporting a 20% contribution.[96] SHG has been observed to decrease at larger lattice constants when irradiated at LSPR,[92] where inter-particle field coupling is diminished. Though SHG from a Fano resonant lattice has been evaluated,[92] irradiation at the LR wavelength for SHG has not been considered.

3.3.2 Plasmonic Emission Analogy

The enabling mechanism was hypothesized to be whether infrared irradiation of a nanostructured metamaterial at the LR, engineered to be twice the plasmon resonance (PR), would support plasmonic emission analogous to SHG. Anticipated conditions necessary for such a process areas were as follows: a) lattice constant and LSPR lie within the polarizable envelope of the nanostructures, b) high absorption at the LSPR, and c) lattice configuration with low

polarization dependence. A schematic representation of this concept is illustrated in Figure 3.1.

Combination of a concentrated electromagnetic field around a plasmonic lattice with a polarizability envelope encompassing harmonic ranges appeared fertile for the generation of the higher energy PR mode from stimulation of the lower energy LR mode, analogous to SHG. Infrared energy incident upon a nanostructured metamaterial at the LR wavelength would stimulate plasmons on each nanostructure, as each nanostructure was polarizable at that wavelength. Intensity of these low-energy plasmons would be dependent upon the absorptive properties of the lattice at the LR; higher LR absorption would be observed when the constituent nanostructures are highly absorptive. A transition to the higher energy PR mode could be realized through a temporary, unattainable transition state between the two attainable resonance modes, a postulate of quantum electrodynamics.

Analytic polarizability descriptions of spheroids have shown that structures exist which exhibit the necessary polarizability envelopes required for such a process. For example, a gold

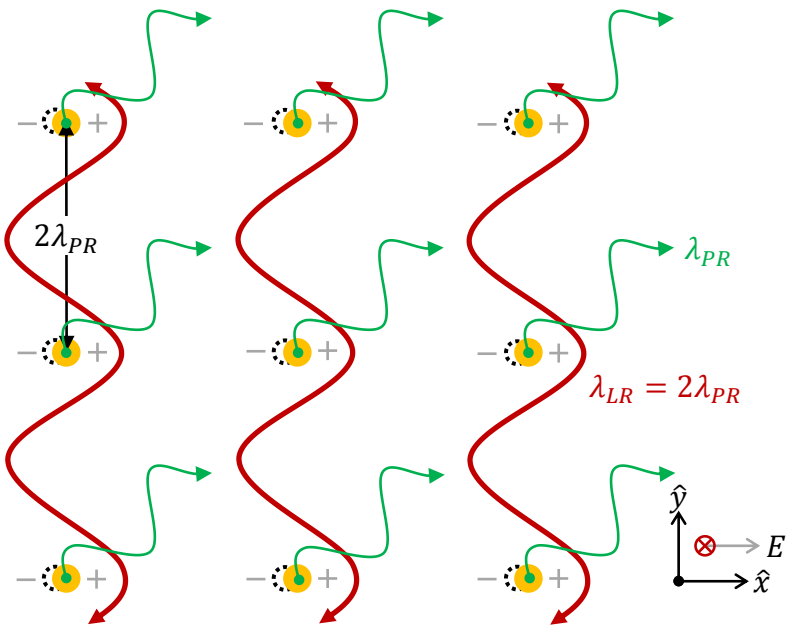

Figure 3.1: A square nanoparticle lattice irradiated at a wavelength equal to the LR, which is engineered to be twice the PR, to support plasmonic emission at the PR.

sphere of 160 nm diameter exhibits a heightened polarizability envelop spanning approximately 400 nm to 900 nm at non-vacuum refractive indices.[98] Such refractive index conditions could be achieved from support of a ceramic substrate, or encasement into an organic thin film. The rapid semi-analytic coupled dipole approximation model could be used to rapidly identify a favorable lattice geometry. This lattice would be further evaluated with a higher order model, such as the discrete dipole approximation, to incorporate substrate effects.

Though analogous to SHG from a conceptual standpoint, it was unclear which, if any, SHG requirements would be needed to observe this process. SHG requires an intense light source, as SHG intensity is directly proportional to the square of pump intensity.[92,93] This is why SHG was not observed until the early 1960s with the development of the maser. It was anticipated that observed intensity of this plasmonic emission would also be directly proportional to incident infrared intensity.[92,99,100] Additionally, SHG requires non-centrosymmetric structures; i.e. perfect spheres, discs, rings, etc. cannot satisfy the necessary conditions. Reported SHG signal arising from centrosymmetric arrays in the literature is mainly attributable from the supporting substrate breaking centrosymmetry and fabrication disorder.[92] Inter-particle spacings comparable to the LSPR have been reported to greatly diminish SHG signal because of less electric field magnitude.[92] However Fano resonant coupling lattices featuring large inter-particle spacings are of direct interest to this hypothesis. It was unclear if any of these effects would play an experimental role due to fundamental differences between SHG and the hypothesis of this work.

3.4 Summary

Theory was developed which describes an opportunity to exchange energy between

resonances using metamaterials with certain geometric criteria to allow infrared energy to be absorbed and emitted at a tunable, higher energy wavelength dictated by the PR. This concept was built upon other resonance exchange mechanisms established in the literature such as plasmon-enhanced transmission and SHG. Using these recognized concepts in conjunction with Kirchhoff's Law of Thermal Radiation, it was anticipated that irradiation of a nanoparticle lattice at the LR could support the emission at the PR, provided the lattice constant is engineered to be twice the PR. Required models to determine proper geometric morphology, metal, and polarizability parameters of a metamaterial to test this hypothesis exist within the NanoBio Photonics Lab.

Chapter 4

FABRICATION & CHARACTERIZATION OF NANOSTRUCTURED METAMATERIALS

Nanostructured metamaterials have widespread applications in nearly every technology sector, and thus a wide variety of fabrication and characterization methods exist for the specific interests of each application. Thermal energy harvesting performance of a metamaterial was anticipated to benefit from large-area fabrication and careful, precise electromagnetic characterization to bridge theory with performance. This chapter outlines the identification and/or development of fabrication and characterization techniques for nanostructured metamaterials which support an energy exchange between resonance frequencies.

4.1 Fabrication of Nanostructured Materials

Metamaterial fabrication is a vast area of research,[101] with each technique having unique advantages and disadvantages. Arrays of randomly arranged structures appear frequently in the literature, whose methods of fabrication are well-understood. However periodic arrays which support diffractive coupling demand control over the inter-particle spacing in addition to particle structure. This requires use of printing/patterning techniques, i.e. lithography, which limits available methods relative to randomized arrays. Common processes which support fabrication of lattices include dip pen nanolithography (DPNL),[102] electron beam lithography (EBL),[103] focused ion beam lithography (FIB),[104] nanoimprint lithography (NIL),[105] and nanosphere lithography (NSL).[106] The unique benefits and drawbacks of these lithography techniques are summarized in Table 4.1.

Method	Principle	Benefits	Drawbacks
DPNL	Ink deposition with AFM cantilever tip	▪ Complex patterns	▪ Substrate use dependent on ink types ▪ Low throughput ▪ Equipment capital
EBL	Mask creation using electron beam to pattern a polymeric resist	▪ Complex patterns ▪ No masks required ▪ Widely used	▪ Low throughout ▪ Conductive substrates ▪ Equipment capital
FIB	Etching of material using beam of ions	▪ Higher resolution over electron beams	▪ Ion implantation ▪ Altered material properties ▪ Equipment capital
NIL	Mask creation using physical imprint of a pre-defined pattern into polymeric resist	▪ High throughput ▪ Consistent pattern between samples ▪ Inexpensive	▪ Requires another lithography method to produce master ▪ Sensitive to substrate defects ▪ Primarily useful for copies of a pattern
NSL	Spheres used to mask areas of substrate during metallization	▪ Large area patterning ▪ Inexpensive ▪ High throughput	▪ Limited lattice types ▪ Limited structure geometries

Table 4.1: Comparison of common lithography techniques used to fabricate lattices of nanostructures

4.1.1 Electron Beam Lithography

EBL is a lithographic process which uses an electron beam to pattern a polymeric resist by altering its solubility. As electrons enter the resist, energy transferred during the electron-polymer collisions break up polymer chains, which increases solubility of the polymer in the exposed areas. These resists are referred to as "positive electron resists." Immersion of the resist into a solvent enables removal of the broken chain clusters, referred to as "developing." After development, the resist features sufficient height contrast between the exposed and non-exposed areas to exhibit a visible pattern. Metallization of this pattern followed by resist liftoff results in nanoparticles whose structure and spacing reflects the pattern of the electron resist.

EBL is a favorable lithographic process for creating multiple structure morphologies and spacings with the low degree of spatial variability necessary for accurate numerical modeling. Additionally, minimal physical processing during the fabrication stages makes EBL favorable in

electron spectroscopy characterization which requires a fragile 50 nm thick substrate prone to breakage. For these experiments, EBL was identified as a key technique because of favorable lithographic resolution and minimal physical handling in comparison to other methods. Sub-Angstrom resolution is possible in EBL because of the picometer-order de Broglie wavelength of electrons in these setups.[107] However, the ultimate resolution of EBL is influenced by equipment factors such as beam spot size, energy distribution of the beam, and beam path aberrations.

A Philips XL40 scanning electron microscope (SEM) was retrofitted with an EBL instrument from Field Emission Inc. (FEI) to generate lattices of complex nanostructures. This setup can achieve an approximate 30 nm lithography resolution, though dependent on electron beam spot size, accelerating voltage, and electron dose. Resist thickness also influences ultimate structure resolution because of its constraint on the metal deposition process. Electron resists such as 2% 495k amu poly(methylmethacrylate) (PMMA) in anisole and ZEP-520A were identified as ideal resists for this technique. The conventional 1:3 solution of ispropanol:MIBK and heated acetone baths for development and liftoff, respectively, were identified as proceeding processes to follow established EBL literature. Multiple metallization techniques have been investigated by the NanoBio Photonics Lab useful for modification of this process to result in various structures.[108]

4.1.2 Nanoimprint Lithography

NIL is a lithographic process which transfers a pattern from one substrate to another by applying physical pressure between a resist and pre-patterned surface (referred to as a "stamp").[105] During pressure application, the resist is heated beyond its glass transition temperature to allow penetration of the pattern features from the stamp into the resist. This allows the resist to cool around the stamp features once pressure is relieved. The stamp is then

peeled from the resist, resulting in a patterned resist ready for development (to remove residual resist) and metallization. Facile separation between the resist and stamp is motivation behind implementing roll-to-roll NIL in industry for high-throughput nanopatterning.[109]

NIL is capable of large area patterning (>> 1cm^2) while maintaining a high throughout relative to other lithographic methods. Large pattern areas are beneficial in optical spectroscopy to increase signal-to-noise ratio and to ease the need for rigorous sample alignment, which complicates experimental setups with additional beam focusing optics and cameras. Intensity of an observable spectral feature exhibited by a nanoparticle lattice is directly dependent on the number of elements within the lattice exhibiting that feature. The number of particles in a given area is typically 10^3 to 10^4 times less in a diffractive coupling lattice than in a random array.[110] Therefore large patterned areas are preferable for accurate optical characterization.

Stamps used during NIL are replicated from a single "master stamp," and are reusable for many lithographic trials. Master stamps are fabricated from the reactive ion etching of a masked silicon substrate, whose mask pattern originates from some other lithography method such as EBL. Master silicon stamps are negatively replicated with poly(dimethylsiloxane) (PDMS) after the patterned silicon is treated with trimethylsilyl chloride (TMCS) for anti-sticking. The flexibility and low-surface energy of PDMS supports facile stamp removal after NIL. To date, master stamps most commonly feature arrays of posts or holes, or line gratings.[105,111–114] Complex structures such as rings and oligomers appear possible as well.

A thermal NIL instrument from NIL Technology was setup to generate 1 cm^2 area nanoparticle lattices on ceramic and organic substrates for optical characterization. This instrument allows application pressures up to 7 bar and temperatures to around 250 ^{o}C. Current NIL methods have reported resolution around 20 nm, though less than 10 nm is achievable

according to reports. Though the type of resist is not critical, PMMA is most commonly used throughout industry and academia.[109] The following NIL parameters were employed to date for successful patterning of cylinders into PMMA over a 1 cm^2 area: 6.6 bar pressure at 200 ˚C for a 20 minute holding time followed by stamp removal at 80 ˚C in 1 bar pressure. Precise characterization of PMMA development using O^2 plasma etching will be required to adopt this process for future work.

4.1.3 Interfacial Reduction of Noble-Metal Salts

Selective reduction of metallic salt solutions suspended onto interfaces of PDMS posts with hydrophobic surface tension appeared to result in ordered lattices of nanoparticles.[115] This ambient condition, bottom-up approach is independent of the metal type - gold, silver, copper, etc. could be used. Furthermore, it could serve as an economic alternative to conventional top-down lithography, which requires high capital, energy intensive equipment in environments not suitable for organics. Balance between thermodynamic and surface forces at a PDMS-redox solution interface governs the ability of different structures to be grown by controlling mass transport characteristics. This process, as conducted in this work, is illustrated in Figure 4.1.

To date, fabrication of rings and/or discs appears to have resulted from this technique by varying the deposition time and redox solution concentration. Gold and silver structure lattices were studied from reduction of 0.5 to 0.005 mass percent hydrogen tetrachloroaurate (TCA) and ammoniacal silver nitrate solutions, respectively.[115] Deposition conditions were approximately 90% humidity at 23 ˚C for times varied between 6 hours and 72 hours. The 0.005 mass percent solutions at 16 to 20 hour deposition times appeared ideal from microscopy and spectroscopic characterization, but validation is subject of ongoing work. The substrates used in these studies were stamps of ordered PDMS posts used for NIL, so additional structures could be possible

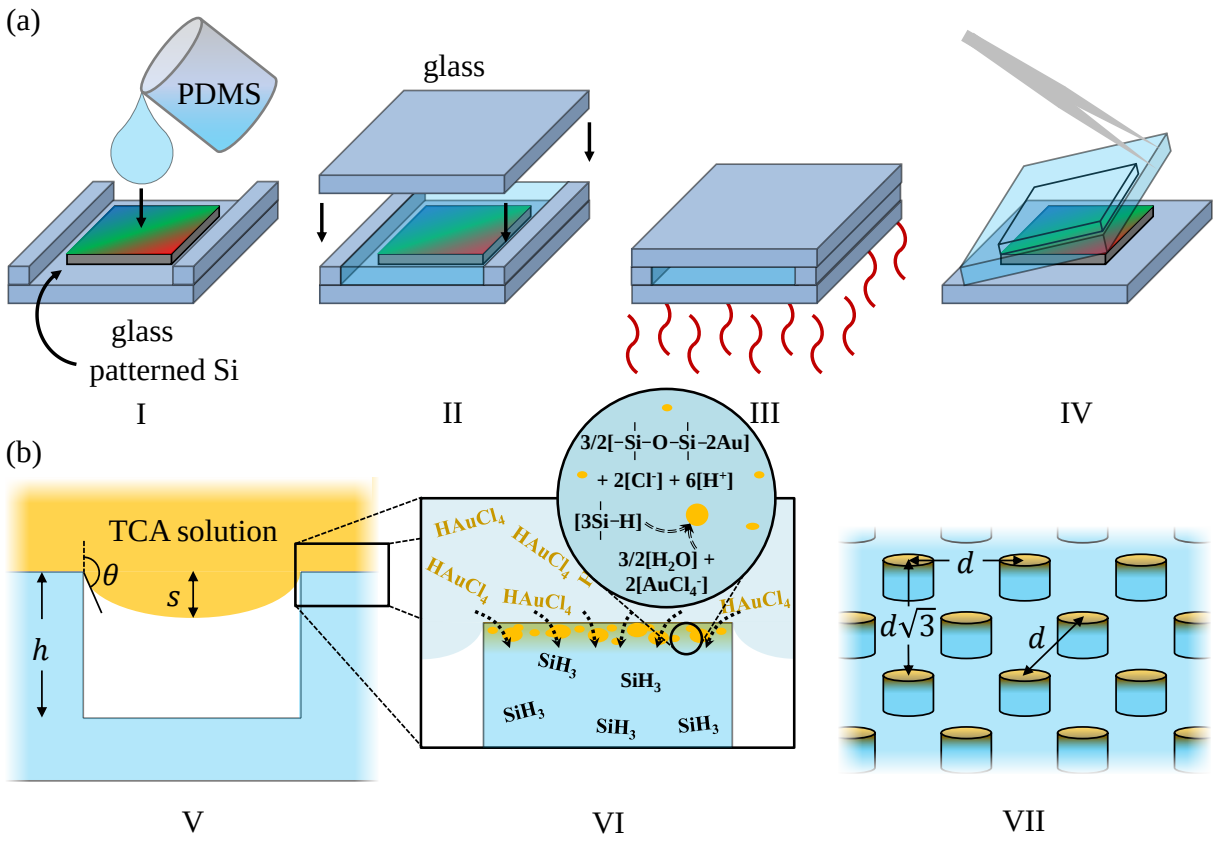

Figure 4.1: Fabrication of a hexagonal gold nanoparticle lattice on a PDMS substrate using interfacial reduction of TCA. (a) A PDMS substrate with a desired pattern of posts is made from a negative-patterned silicon wafer via thermal imprint replication. (b) Patterned PDMS is exposed to a metallic salt solution, TCA in this case, to reduce gold nanoparticles onto the posts.

with alternate PDMS patterning. Validation of ordering nanoparticles with this approach is subject of ongoing efforts within the NanoBio Photonics Lab.

4.2 Electron Microscopy

An electron microscope uses a beam of electrons to provide images below the optical diffraction limit, and remains a key spatial and elemental characterization tool since their inception in 1931.[116] Images are constructed from the energy losses and spatial displacement patterns of electrons recovered from an incident electron beam used to probe a sample. Resolution of an electron microscope exceeds optical methods because electron wavelengths are

5 orders of magnitude less than photons, overcoming the optical diffraction limit. The de Broglie wavelength of electrons dictate the resolution of an electron beam, though factors such as stage vibration preclude achieving such low resolution.

Each type of electron microscope is comprised of the same basic components: an electron gun, condenser lens, objective lens, sample stage, and detector.[117] The basic schematic of an electron microscope is shown in Figure 4.2. Electron beams are generated using a thermionic or field emission gun; field emission types are most commonly used for beam uniformity and heating considerations.[117] Emitted electrons pass through a condenser lens into the objective

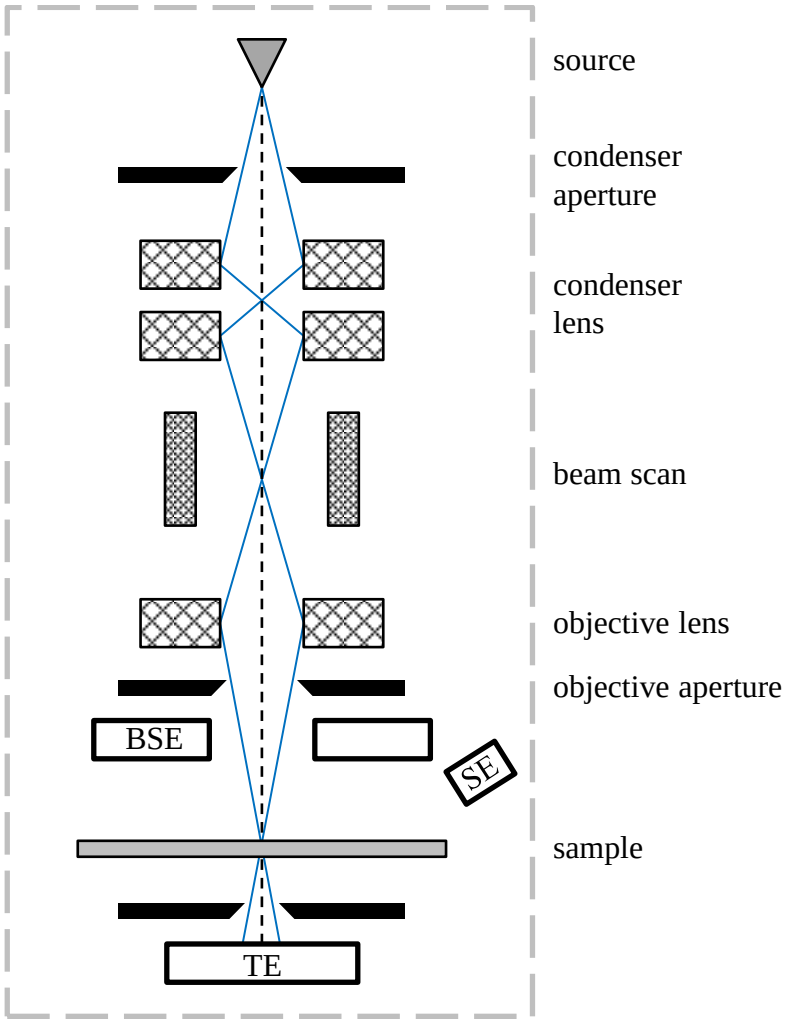

Figure 4.2: Schematic of an electron microscope.

lens, which is used to focus the beam onto the sample. In-plane movement of the objective lens allows scanning of the electron beam over the sample in a raster pattern. Differences between microscope types lay in respective electron detection methods.[107,117] This section outlines experimental considerations of electron microscopy, and identifies unique uses for each detection method in this work.

4.2.1 Scanning Electron Microscope

A scanning electron microscope (SEM) is an electron microscope that generates images from inelastically scattered electrons collected above the sample, as shown in Figure 4.2. These images provide surface topography and spatial information of structures useful for fabrication optimization and numerical modeling. Kinetic energy carried by the incident beam results in a scattering signal of secondary electrons, which are collected, analyzed, and compared to the incident beam energy provide such images.[117] Signal from secondary electrons (SE) is distinguishable from elastic back-scattered electrons (BSE) by their difference in kinetic energy. Because energy is lost from the incident beam to the sample, electron charge-buildup occurs in non-conductive samples. This can result in images with elongated features which do not reflect reality, lack of contrast, and focusing difficulties in organic samples. Lower energy electron beams around 5 keV can combat charging issues at the cost of resolution. These imaging problems are not present for conductive samples which can be subjected to beam energies of 30 keV or higher.

4.2.2 Transmission Electron Microscope

A transmission electron microscope (TEM) is an electron microscope that generates images from the detected electrons which transmit through the sample (TE) , as shown in Figure 4.2.[117] The image produced by a TEM is based on absorption of electron current within the

sample. These images can provide chemical/material properties, electromagnetic behavior, and spatial information of a sample immersed in some media. For example, viruses and other biological samples can only be analyzed within water. This would be particularly useful for nanoparticle lattices embedded into an organic matrix. A TEM must be used to analyze such samples because the smooth organic surface precludes useful information from SEM imaging. Drawbacks to TEM compared to SEM characterization include constraints on sample type and fabrication makeup. Samples subject to SEM are not (generally) constrained by their dimensions or materials. However, TEM restricts sample thickness and substrate material. Thickness is generally limited to a few hundred nanometers, though this can be much lower in some cases,[107,118] making them sensitive to physical handling. The substrate supporting a nanoparticle lattice must be transparent to electrons, such as 50 nm thick silicon nitride membranes, with specific area windows for the lattice. These considerations support use of EBL to generate samples which will be subjected to TEM characterization because of their fragile substrates.

4.3 Electron Energy Loss Spectroscopy

The analysis of an energy loss distribution of electrons accelerated through a sample is referred to as electron energy loss spectroscopy (EELS), which can map energy loss pathways and plasmon modes of a nanostructure.[118] EELS is performed in a TEM by sweeping the energy of a sub-nanometer diameter electron beam while raster scanning across the area of a metallic nanostructure.[119] Transmitted electrons are sorted by a magnetic prism beneath the sample, causing angular deflection according to a loss in energy. Energy loss maps can be generated using EELS by plotting the intensity of lost energy at a particular value over the whole nanostructure. This can be performed at energies corresponding to various plasmon modes (dipole, quadrupole, etc.),[119,120] and therefore provides information of energy loss pathways for

that nanostructure. Resonance energies of these plasmon modes can be extracted and compared directly to optical stimulation. Interestingly, plasmons were first discovered when energy losses were observed in reflected electrons from aluminum.[121] EELS may provide additional understanding of SHG from structures with varying degrees of non-centrosymmetry in this work.

4.3.1 Energy Loss Spectra

Energy loss spectra obtained from EELS is comprised of three sub-regions: the high-loss region (inner-shell interactions), the low-loss region (valence-band interactions), the zero-loss region (transmitted electrons).[118] Plasmonic activity is observed in the low-loss region, near the zero-loss feature. Electrons which experience little to no energy loss when traveling through the sample comprise the zero-loss feature at 0 eV. The breadth of this feature reflects the energy distribution of the electron beam.[118] Remaining features within the low-loss region reflect interactions with the valence electrons of the metallic nanostructure, i.e. electron plasma.

EELS experimentation can be difficult to perform when the area of interest involves the low-loss region. Signal resolution can be hampered by spectrometer saturation at the zero-loss peak, leading to low exposure times and low signal-to-noise ratio. Energies between 0.8 eV and 3 eV are of particular interest when performing EELS on plasmonic nanostructures. However, breadth of the zero-loss peak commonly encompasses this region, making it difficult to extract plasmon resonance modes if a proper reference spectrum is not obtained.

4.3.2 Plasmon Spectroscopy

Spectra generated by EELS are related to results obtained by optical spectroscopy, though there is not direct correspondence between the two. This is because the mechanisms for energy transfer from inelastic collisions of photons and electrons are different.[118] When a photon is absorbed, transfer of momentum is described by its wavelength. Momentum transferred by an

electron is described by its scattering angle. This can result greater momentum transfer from electrons as compared to photons. This fundamental difference in excitation permits plasmonic dark modes to be observed using electrons.[107] These modes are referred to as dark because the zero net dipole moment precludes coupling with photons.

Mapping plasmon modes using EELS is possible because the charge of an incident electron interacts with conduction electrons on a nanostructure in a similar fashion to the electric field of a photon.[118,119] Negative charge of the electron repulses the electron gas in the metal, creating a positive hole in the charge density.[118] Energy needed to create this charge void is referred to as a plasmon energy, E_p. Plasmons carry a quantum of energy, so discrete multiples of E_p may be observed for the same oscillation modes in EELS spectra.[118]

EELS can be numerically modeled using the DDA in order to facilitate interpretation of experimental results. Available code, such as DDEELS,[122] replaces the photon plane wave excitation used in DDSCAT with a point electron source, supporting compatibility with pre-generated DDA targets for nanostructures of interest. Code has also been developed within the NanoBio Photonics Lab research group to permit two-dimensional target generation from SEM images of fabricated structures. This is expected to allow closer correlation of experimental EELS spectra to theoretical models for this work.

4.4 Optical Spectroscopy

Electromagnetic behavior of metamaterials under optical stimulation can be characterized using optical spectroscopy.[123,124] Optical spectroscopy measures the intensity of some optical signal representing an energy pathway as a function of incident photon wavelength. This section

overviews the development (§ 4.4.1) and identification (§ 4.4.2) of optical spectroscopy methods that will be used for electromagnetic characterization in this work.

4.4.1 Measuring Optical Attenuation

A novel combination of traditional transmission spectroscopy[124] and an integrating sphere provided a bi-directional energy balance to observe light trapping in nanostructured metamaterials, and will be a key tool in future work. Figure 4.3 outlines the layout of this apparatus. Irradiation of an isolated nanoparticle ($a \ll \lambda$) results in Mie[73] and/or Rayleigh scattering,[125] or resonant plasmonic absorption, whose outcomes include thermalization[40] or reradiation.[126] Introduction of geometric substrates ($a \gg \lambda$) to support such nanoparticles convolutes these energy pathways with classical forward scattering (i.e. transmission), back scattering (i.e. reflection), and bulk absorption.[125] This convolution gives rise to two distinct experimental observables: transmission (T) and reflection (R). Photon energy trapped within the metamaterial was referred to as attenuation, which consisted of thermalized plasmons from

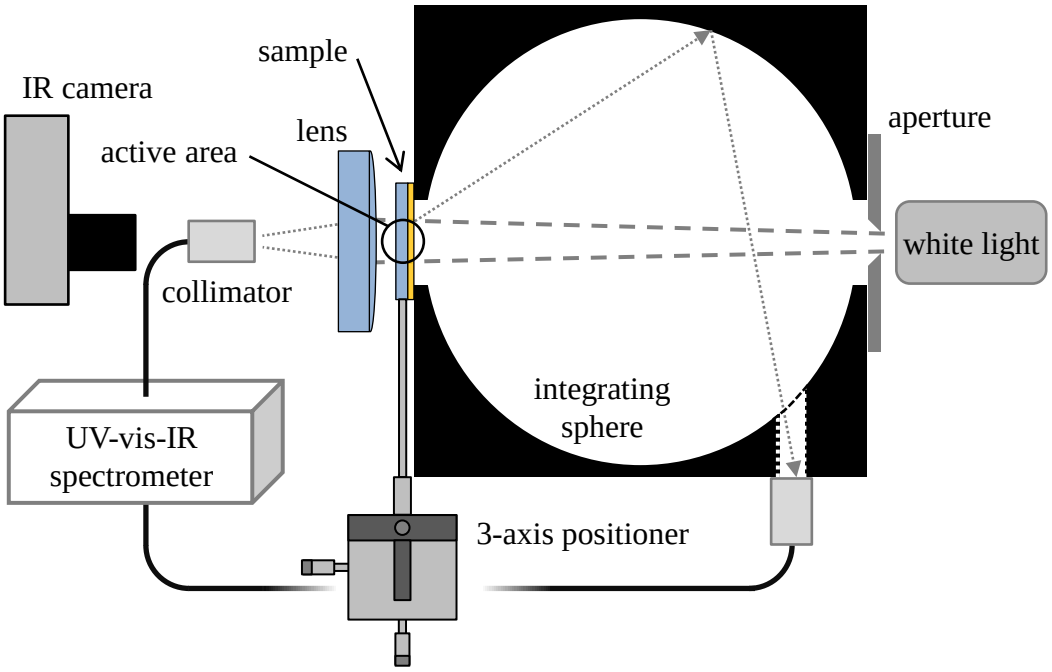

Figure 4.3: Spectroscopy apparatus for measurement of spectral attenuation of a metamaterial.

absorption, bulk material absorption, and oblique scatterers trapped within the material.[127] Attenuation was calculated as:

$$A = 1 - (T + R) \tag{4.1}$$

The apparatus in Figure 4.3 measured T and R with a fiber-coupled spectrometer to detect spectra in the forward and reverse directions. An infrared camera directly measured thermalized plasmons, which caused a bulk temperature rise in the host substrate of samples. Distinction between plasmonic absorption from measured A was possible using *a priori* Mie theory[73] or Beer-Lambert absorption coefficient for nanoparticles.[128] For two-dimensional nanoparticle arrays without inter-particle interactions, absorption was shown to account for 90% of measured attenuation with resonant irradiation using Mie theory.[127] However samples with three-dimensional dispersions, such as metal-polymer nanocomposites, absorption was found to constitute approximately 1/3 of measured attenuation using finite element analysis.[128]

A beam size of approximately 3 mm in diameter constrained this apparatus to measurement of samples with large areas of a particular pattern. Therefore, only samples fabricated using NIL or interfacial reduction yielded results which reflected their respective nanostructuring, due to their large-area patterns. Samples fabricated using EBL generally had too small of a patterned area (~ 0.25 mm^2) to encompass the probing beam, which made it difficult to distinguish observed optical behavior of the patterned lattice from surrounding background films, defects, etc. Reductions in beam size were possible with the mechanical aperture in Figure 4.3 at the cost of beam intensity (and extensively, signal-to-noise ratio) or additional focusing optics, but were not used in this work. Improvements to signal resolution, beam size, and sample compatibility in this system are subject of ongoing work in the NanoBio Photonics Lab.

4.4.2 Detection of Plasmonic Emission

Plasmonic emission in the visible to near-infrared spectra from lower-energy stimulation as hypothesized in this thesis was seen as an analog to second harmonic generation (SHG). Experimental observation of plasmonic emission was therefore anticipated to require an apparatus similar to SHG studies, comprised of a transmission spectroscopy setup modified with light modulation elements and high gain, low noise detector (e.g. photomultiplier tube (PMT)). Table 4.2 summarizes setups and conditions employed in the literature to observe SHG from nanoparticles. Unfortunately, SHG efficiency is difficult to extract from the literature to anticipate signal strength of plasmonic emission. SHG is generally reported in an arbitrary, unit-less quantity whose intensity is unique to a particular detection setup. McMahon *et al*. reported a signal enhancement from ~ 1,500 counts/second to ~ 500,000 counts/second of SHG by carefully matching the LSPR to the source,[94,95] the only quantified indication of potential emission signal.

Reference	Fundamental	Incidence	Sample Area	Detection
Walsh[93]	Ti:Sapphire laser 80 mW, 100 fs pulse, 20 MHz	67 Hz chopper, 50 µm Ø	50 µm circular	objective lens, filter PMT, lock-in amp, monochromator
Capretti[92]	Ti:Sapphire laser 40 mW, 120 fs pulse, 10 MHz	$\theta_i = 45^\circ$ incidence for specular SHG	50 µm circular	objective lens, filter, chopper, lock-in amp, monochromator, PMT
Kujala[96]	Nd:glass laser 350 mW, 200 fs pulse, 82 MHz	$\theta_i \leq 2^\circ$ incidence for T and R SHG, 200 µm Ø	1 mm^2 square	filter, chopper, lock-in amp, PMT
Butet[100] Bachelier[129]	Ti:Sapphire laser 300 mW, 180 fs pulse, 76 MHz	130 Hz chopper, harmonic filter	cuvette cell	filter, monochromator, PMT, 130 Hz chopper, photon counter, 80 s integration
McMahon[94] McMahon[95]	Ti:Sapphire laser 250 - 500 mW, 50 fs pulse, 93 MHz	50 µm Ø to array substrate	60 µm x 60 µm	objective lens, monochromator, PMT, photon counter
Sandrock[130]	Ti:Sapphire laser 24 mW, 150 fs pulse, 80 MHz	$\theta_i = 0^\circ$ - 40°	Au-Al composite film	filter, monochromator, PMT, photon counter, 1 s integration

Table 4.2: Summary of experimental apparatus parameters used to observe SHG.

The setup in Figure 4.4 was designed based on previous SHG studies to detect plasmonic emission from a resonance exchange. It was described in § 3.3.2 that polarized infrared photons would be required to irradiate the nanostructured metamaterial for the emission of higher energy photons, whose wavelength was dictated by the plasmon resonance (PR). An infrared filter was introduced in the beam path to filter out intense, infrared signal from the harmonic signal prior to the detection setup. The detection setup consisted of a fiber-coupled monochromator tuned to the PR, and a PMT or avalanche diode (semiconducting alternative to PMTs). These high-gain, low noise detectors were identified as primary options because plasmonic emission is anticipated to exhibit power densities on the order of SHG. A CCD camera and removable mirror was integrated to view sample alignment through a 100x microscope objective. A 3-axis micropositioner supported tunable alignment and repeatable focal distances.

Use of a Ti:Sapphire laser was incorporated into the design because of its controllable pulse width and tunable wavelength range into the near infrared spectrum. A tunable wavelength range made this apparatus amenable to different samples, each with a unique lattice resonance (LR) wavelength. The Ti:Sapphire laser at the University of Arkansas Nano-Bio Materials

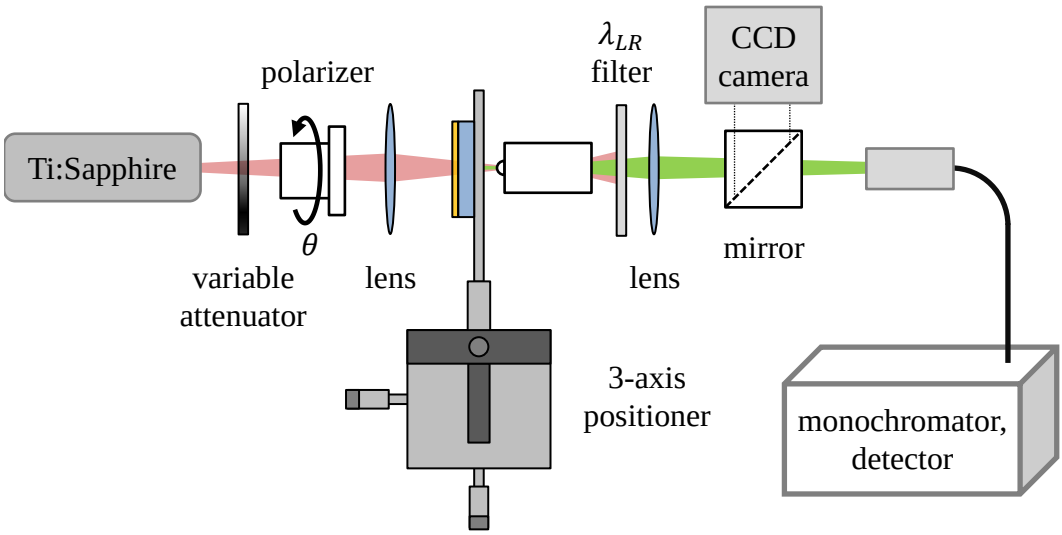

Figure 4.4: Spectroscopy apparatus for designed for detection of plasmonic emission from a nanostructured metamaterial under infrared irradiation.

Characterization Facility was found to have an upper wavelength limit of 1300 nm. This limited future lattice designs to those which satisfy the $2\lambda_{PR}$ < 1300 nm condition. Samples exceeding this wavelength limit would have required an infrared diode-pumped laser with pulse modulation elements, which limits the apparatus to that unique sample.

4.5 Summary

Fabrication and characterization methods including NIL, EBL, SEM, EELS, and optical spectroscopy were identified and developed to study nanostructured metamaterials. A new fabrication method to embed nanostructure lattices into biocompatible PDMS thin films, such as interfacial reduction, was studied. SEM was identified to provide spatial and structural characterization necessary for numerical modeling. A custom setup built around an integrating sphere was developed to measure far-field optical attenuation and extinction spectra. EELS was anticipated to correlate lack of centrosymmetry in fabricated structures to observed plasmonic emission behavior. A transmission optical spectroscopy apparatus modified with a Ti:Sapphire laser and a high gain, low noise detector, such as a PMT or avalanche diode, was designed to detect plasmonic emission. The wavelength range of the source used in this apparatus design constrained future samples to those which satisfy the $2\lambda_{PR}$ < 1300 nm condition. These experimental methods and tools provided a foundation for the fabrication and characterization of nanostructure metamaterials anticipated to support an exchange of resonance.

Chapter 5

CONCLUDING REMARKS

The research described in this thesis has examined the concept, design considerations, fabrication, and characterization of nanostructured metamaterials which support exchange of resonance for infrared harvesting. A polarizability-extraction technique was employed to model the electromagnetic behavior of diffractive coupling nanoring lattices over a range of geometric parameters to support rational design of nanostructured metamaterials. Theory supporting an exchange of resonant energy in diffractive coupling lattices was developed. Electron beam and nanoimprint lithography techniques were identified in addition to the development of interfacial reduction as methods for fabricating metamaterials for characterization experiments. Electron microscopy techniques to provide structural data for numerical modeling were summarized. Optical spectroscopy systems were developed for electromagnetic characterization. This chapter will summarize the overall goal of research, findings to date, and ongoing work in pursuit of nanostructured metamaterials for thermal energy harvesting.

5.1 Importance of Work

Harvesting radiated infrared energy for opto-plasmonic functionality could lay a foundation for next-generation photonic logic device architectures. Conventional electronic devices are powered primarily by 40% efficient fossil fuel processes,[7,8] leaving 10 terawatt of global thermal energy for potential recycling.[3,8] A reduction in electronic device power consumption could lower energy production demands, and extensively, carbon emissions.[1,7] Solid-state, emission-free recycling of dissipated thermal energy into electronic and/or photonic

signals is of interest to the transportation, electronics, industrial, and biological industries. For example, conversion of dissipated heat from electronic processors could enable facile integration of photonic interconnects for improved clock-speeds by re-radiating infrared energy as visible light.[14,15,25] Conventional electronic interconnects comprise nearly 80% of processor power consumption.[25] The proposed concept addresses recovery and utilization of waste radiative heat for advancing remote power generation, photonic circuitry, and wearable sensor technologies.

5.2 Summary of Findings

A hypothesis was proposed which describes an opportunity for the exchange of resonant energy between the plasmon resonance (PR) and lattice resonance (LR) modes of a nanostructure lattice. Infrared irradiation at the LR, engineered to be twice the PR, was established as a possible mechanism for emission at the PR provided that the two resonances lay within the polarizability envelope of the lattice. Plasmonic emission from this process was considered to be analogous to second harmonic generation (SHG), and supported by Kirchoff's Law of Thermal Radiation and observations of plasmon-enhanced transmission.

Models were developed to support rational design of nanostructured metamaterials, with a focus on ring structures. Diffractive coupling nanoring lattices were simulated with the help of P. Blake and D. DeJarnette over a multitude of geometric values to optimize their optical absorption and extinction. The discrete dipole approximation (DDA) was used to show modulation of radius primarily determined the localized surface plasmon resonance (LSPR) wavelength and breadth, while wall-thickness primarily influenced the absorptive behavior and tuned the LSPR wavelength. Extraction of particle polarizability from the DDA using code modifications made by P. Blake enabled rapid coupled dipole approximation (CDA) modeling of

nanoring lattices using a procedure developed with the help of D. DeJarnette. Modulation of the lattice constant elicited a 4-fold enhancement of plasmon resonance magnitude by considering particle polarizability. These simulations provided a guide for design of nanoring lattices, and amenable approach for other nanostructure lattices, in future experiments.

Electron beam (EBL) and nanoimprint (NIL) lithography, and interfacial-reduction were identified as particular techniques of interest for fabricating nanostructured metamaterials. The interfacial reduction method appeared to deposit ordered nanostructures onto poly(dimethylsiloxane) (PDMS) films. This ambient environment, self-assembly method involved the controlled reduction of noble-metal salts at PDMS interfaces dictated by the surface hydrophobicity of patterned PDMS posts. Hydrogen tetrachloroaurate (TCA) and ammoniacal silver nitrate solutions were prepared by J.R. Dunklin and X. Wei according to their previous research to produce gold and silver structures, respectively. A reproducible method developed with help of J. Proctor for PDMS replication of patterned silicon had enabled rapid progress of these experiments.

Electron microscopy and optical, as well as electron, spectroscopy methods were examined and developed for characterization of nanostructured metamaterials. A bi-directional spectroscopy apparatus for measuring optical attenuation of metamaterials was built around an integrating sphere. Measured attenuation was found to consist of approximately 90% plasmonic absorption in two-dimensional arrays. The capabilities of this system were expanded with the help of C. Chambers, C. Bodinger, and J.R. Dunklin to include white light, beam focusing optics, and an infrared camera. Another spectroscopy apparatus was designed to experimentally observe plasmonic emission, based on reported apparatuses in the literature from SHG studies. This system was anticipated to test the proposed resonance exchange hypothesis.

5.3 Current and Future Work

The resonance exchange hypothesis of this thesis will be tested using a square lattice of nanospheres. Spheres will be used due to their geometric simplicity and well-understood behavior in lattices, as previous evaluation of 160 nm gold spheres indicated a polarizability envelope sufficient to support a harmonic.[98] Analytic polarizability descriptions could support identification of other geometries. Fano resonant coupling lattices with gold spheres of 160 nm size have been fabricated in the NanoBio Photonics Lab using EBL, though with lattice constants less than that of interest to the hypothesis. Plasmonic emission will be tested using the apparatus identified in § 4.4.2 under the advisement of the Arkansas Nano-Bio Materials Characterization Facility. Positive results from these experiments will lead to evaluation of more complex ring structures in the same fashion.

The polarizability extraction technique for modeling lattices of complex nanostructures has been validated for rings, but other shapes have yet to be considered. Results for simple shapes, e.g. ellipsoids, whose polarizability was extracted from the DDA will be compared with results arising from their analytic polarizability. Further evaluation of the modeling technique is important to identify any differences which follow a trend between the CDA and higher order models. Conscious knowledge of the advantages and drawbacks, including consistent differences between models, of this method supports realization of envisioned resonance features to experimentally observed spectra in prototype metamaterials.

Nanoring lattices modeled to date reflect smooth, ideal structures not obtainable in a lab frame. Previous modeling approaches with the DDA will be used to evaluate optical behavior of rings comprised of tiny grains, arising from electroless gold plating metallization. Preliminary results by M. Lisunova suggest that extinction spectra will be comparable, but a higher

absorption-to-scattering ratio will be observed.[131] This is hypothesized to be a result of the 30 nm spherical grains prevalent in electroless plating which are primarily absorptive, according to Mie theory. Effects of lattice constant disorder will also be investigated using CDA code implemented by J.C. Norman.

Identification of optimal exposure conditions to control nanoparticle nucleation and structure growth during interfacial reduction is the subject of ongoing work with J.R. Dunklin. An understanding of ideal salt solution concentration, exposure time, and PDMS substrate preparation are vital to advancing this technique. The resultant structure types are currently unknown, though suspected to be disk or ring-disk hybrid structures. Unfortunately, electron microscopy techniques are unable to distinguish these structures from the host substrate. Computational CDA and DDA approaches are being employed to correlate experimental spectra with structure types and lattice conditions assumed by models.

BIBLIOGRAPHY

1. S. Chu and A. Majumdar, "Opportunities and challenges for a sustainable energy future," Nature **488**, 294–303 (2012).

2. International Energy Agency, *World Energy Outlook 2013* (2013).

3. U.S. Energy Information Administration, *Annual Energy Review 2011* (2012).

4. C. J. Vineis, A. Shakouri, A. Majumdar, and M. G. Kanatzidis, "Nanostructured thermoelectrics: big efficiency gains from small features," Adv. Mater. **22**, 3970–3980 (2010).

5. L. E. Bell, "Cooling, heating, generating power, and recovering waste heat with thermoelectric systems," Science **321**, 1457–1461 (2008).

6. M. Maldovan, "Sound and heat revolutions in phononics," Nature **503**, 209–217 (2013).

7. R. Segalman, J. Urban, and K. See, *Solution-Based Hybrid Thermoelectric Materials* (2013).

8. A. I. Hochbaum, R. Chen, R. D. Delgado, W. Liang, E. C. Garnett, M. Najarian, A. Majumdar, and P. Yang, "Enhanced thermoelectric performance of rough silicon nanowires," Nature **451**, 163–167 (2008).

9. R. Lee, "The outlook for population growth," Science **333**, 569–573 (2011).

10. A. Bonnabel and Y. de Charentenay, "Energy harvesting market will approach $ 250M in five years , with fastest growth from thin film thermal technologies," MEMS' Trends 22–24 (2012).

11. G. Min, "Thermoelectric Energy Harvesting," in *Energy Harvesting 2011* (Engineering and Physical Sciences Research Council, 2011).

12. P. Patel, "Powering Your Car with Waste Heat," http://www.technologyreview.com/news/424092/powering-your-car-with-waste-heat/.

13. C. B. Vining, "An inconvenient truth about thermoelectrics," Nat. Mater. **8**, 83–85 (2009).

14. E. Ozbay, "Plasmonics: merging photonics and electronics at nanoscale dimensions," Science **311**, 189–193 (2006).

15. M. L. Brongersma and V. M. Shalaev, "The case for plasmonics," Science **328**, 440–441 (2010).

16. X. Liu, T. Tyler, T. Starr, A. F. Starr, N. M. Jokerst, and W. J. Padilla, "Taming the blackbody with infrared metamaterials as selective thermal emitters," Phys. Rev. Lett. **107**, 045901 (2011).

17. C. Wu, B. Neuner III, J. John, A. Milder, B. Zollars, S. Savoy, and G. Shvets, "Metamaterial-based integrated plasmonic absorber/emitter for solar thermo-photovoltaic systems," J. Opt. **14**, 024005 (2012).

18. P. Bermel, M. Ghebrebrhan, M. Harradon, Y. X. Yeng, I. Celanovic, J. D. Joannopoulos, and M. Soljacic, "Tailoring photonic metamaterial resonances for thermal radiation," Nanoscale Res. Lett. **6**, 549 (2011).

19. A. Lenert, D. M. Bierman, Y. Nam, W. R. Chan, I. Celanović, M. Soljačić, and E. N. Wang, "A nanophotonic solar thermophotovoltaic device," Nat. Nanotechnol. **9**, 126–130 (2014).

20. S. Y. Lin, J. Moreno, and J. G. Fleming, "Three-dimensional photonic-crystal emitter for thermal photovoltaic power generation," Appl. Phys. Lett. **83**, 380 (2003).

21. J. A. Paradiso and T. Starner, "Energy Scavenging for Mobile and Wireless Electronics," IEEE Pervasive Comput. **4**, 18–27 (2005).

22. J. M. Gilbert and F. Balouchi, "Comparison of energy harvesting systems for wireless sensor networks," Int. J. Autom. Comput. **5**, 334–347 (2008).

23. R. R. Fletcher, S. Tam, O. Omojola, R. Redemske, and J. Kwan, "Wearable sensor platform and mobile application for use in cognitive behavioral therapy for drug addiction and PTSD," in *Annual International Conference of the IEEE Engineering in Medicine and Biology Society* (2011), Vol. 2011, pp. 1802–1805.

24. R. Matthews, N. J. McDonald, P. Hervieux, P. J. Turner, and M. A. Steindorf, "A wearable physiological sensor suite for unobtrusive monitoring of physiological and cognitive state," in *Annual International Conference of the IEEE Engineering in Medicine and Biology Society* (2007), pp. 5276–5281.

25. D. Miller, "Device requirements for optical interconnects to silicon chips," Proc. IEEE **97**, 1166–1185 (2009).

26. D. Liang and J. E. Bowers, "Recent progress in lasers on silicon," Nat. Photonics **4**, 511–517 (2010).

27. J. Gorrell, M. Davidson, M. E. Maines, L. Gasparov, and P. Hart, "Structures and methods for coupling energy from an electromagnetic wave," U.S. patent US7253426 (2007).

28. J. Gorrell, M. Davidson, and M. E. Maines, "Coupled nano-resonating energy emitting structures," U.S. patent US7361916 (2008).

29. J. Gorrell, J. Tokarz, M. E. Maines, and M. Davidson, "Plasmon wave propagation devices and methods," U.S. patent US7573045 (2009).

30. J. Gorrell, M. Davidson, and M. E. Maines, "Electron beam induced resonance," U.S. patent US7714513 (2010).

31. J. A. Schuller, E. S. Barnard, W. Cai, Y. C. Jun, J. S. White, and M. L. Brongersma, "Plasmonics for extreme light concentration and manipulation," Nat. Mater. **9**, 193–204 (2010).

32. O. Benson, "Assembly of hybrid photonic architectures from nanophotonic constituents," Nature **480**, 193–199 (2011).

33. J. Z. Zhang and C. Noguez, "Plasmonic optical properties and applications of metal nanostructures," Plasmonics **3**, 127–150 (2008).

34. W. L. Barnes, A. Dereux, and T. W. Ebbesen, "Surface plasmon subwavelength optics," Nature **424**, 824–830 (2003).

35. P. K. Jain, K. S. Lee, I. H. El-Sayed, and M. A. El-Sayed, "Calculated absorption and scattering properties of gold nanoparticles of different size, shape, and composition: applications in biological imaging and biomedicine," J. Phys. Chem. B **110**, 7238–7248 (2006).

36. S. Link and M. A. El-Sayed, "Size and temperature dependence of the plasmon absorption of colloidal gold nanoparticles," J. Phys. Chem. B **103**, 4212–4217 (1999).

37. C. L. Nehl and J. H. Hafner, "Shape-dependent plasmon resonances of gold nanoparticles," J. Mater. Chem. **18**, 2415–2419 (2008).

38. C. J. Orendorff, T. K. Sau, and C. J. Murphy, "Shape-dependent plasmon-resonant gold nanoparticles," Small **2**, 636–639 (2006).

39. J. R. Lombardi and R. L. Birke, "A unified approach to surface-enhanced Raman spectroscopy," J. Phys. Chem. C **112**, 5605–5617 (2008).

40. D. K. Roper, W. Ahn, and M. Hoepfner, "Microscale heat transfer transduced by surface plasmon resonant gold nanoparticles," J. Phys. Chem. C **111**, 3636–3641 (2007).

41. G. Baffou, R. Quidant, and F. J. García de Abajo, "Nanoscale control of optical heating in complex plasmonic systems," ACS Nano **4**, 709–716 (2010).

42. D. Pissuwan, S. M. Valenzuela, and M. B. Cortie, "Therapeutic possibilities of plasmonically heated gold nanoparticles," Trends Biotechnol. **24**, 62–67 (2006).

43. H. A. Atwater and A. Polman, "Plasmonics for improved photovoltaic devices," Nat. Mater. **9**, 205–213 (2010).

44. J. N. Anker, W. P. Hall, O. Lyandres, N. C. Shah, J. Zhao, and R. P. Van Duyne, "Biosensing with plasmonic nanosensors," Nat. Mater. **7**, 442–453 (2008).

45. D. K. Roper, W. Ahn, B. Taylor, and A. G. D. Asen, "Enhanced spectral sensing by electromagnetic coupling with localized surface plasmons on subwavelength structures," IEEE Sensors **10**, 531–540 (2010).

46. K. M. Mayer and J. H. Hafner, "Localized surface plasmon resonance sensors," Chem. Rev. **111**, 3828–3857 (2011).

47. B. Auguié and W. Barnes, "Collective resonances in gold nanoparticle arrays," Phys. Rev. Lett. **101**, 143902 (2008).

48. D. DeJarnette, D. K. Roper, and B. Harbin, "Geometric effects on far-field coupling between multipoles of nanoparticles in square arrays," J. Opt. Soc. Am. B **29**, 88–100 (2012).

49. D. DeJarnette, J. Norman, and D. K. Roper, "Spectral patterns underlying polarization-enhanced diffractive interference are distinguishable by complex trigonometry," Appl. Phys. Lett. **101**, 183104 (2012).

50. E. M. Hicks, S. Zou, G. C. Schatz, K. G. Spears, R. P. Van Duyne, L. Gunnarsson, T. Rindzevicius, B. Kasemo, and M. Käll, "Controlling plasmon line shapes through diffractive coupling in linear arrays of cylindrical nanoparticles fabricated by electron beam lithography," Nano Lett. **5**, 1065–1070 (2005).

51. B. Auguié and W. L. Barnes, "Diffractive coupling in gold nanoparticle arrays and the effect of disorder," Opt. Lett. **34**, 401–403 (2009).

52. P. Blake, J. Obermann, B. Harbin, and D. K. Roper, "Enhanced nanoparticle response from coupled dipole excitation for plasmon sensors," IEEE Sensors **11**, 3332–3340 (2011).

53. J.C. Norman and D. K. Roper, "Small displacements perturb Fano coupling for large, ordered nanoparticle arrays." *To Be Submitted*.

54. K. Yee, "Numerical solution of initial boundary value problems involving Maxwell's equations in isotropic media," IEEE Trans. Antennas Propag. **14**, 302–307 (1966).

55. B. T. Draine, "The discrete-dipole approximation and its application to interstellar graphite grains," Astrophys. J. **333**, 848–872 (1988).

56. B. T. Draine and P. J. Flatau, "Discrete-dipole approximation for scattering calculations," J. Opt. Soc. Am. A **11**, 1491–1499 (1994).

57. D. Gutkowicz-Krusin and B. T. Draine, "Propagation of Electromagnetic Waves on a Rectangular Lattice of Polarizable Points," http://arxiv.org/abs/astro-ph/0403082 (2004).

58. B. T. Draine and P. J. Flatau, "Discrete-dipole approximation for periodic targets: theory and tests," J. Opt. Soc. Am. A **25**, 2693–2703 (2008).

59. P. J. Flatau and B. T. Draine, "Fast near field calculations in the discrete dipole approximation for rectangular rectilinear grids," Opt. Express **20**, 1247–1252 (2012).

60. P. Blake, "Refractive Index Chemical Sensing with Noble Metal Nanoparticles," Ph.D. Dissertation, University of Arkansas (2012).

61. J. Kennedy, *A Fast Bresenham Type Algorithm For Drawing Circles* (2012).

62. J. C. Norman, D. F. DeJarnette, and D. K. Roper, "Polylogarithm-based computation of Fano resonance in arrayed dipole scatterers," J. Phys. Chem. C **118**, 627–634 (2014).

63. D. DeJarnette, P. Blake, G. T. Forcherio, and D. K. Roper, "Far-field Fano resonance in nanoring arrays modeled from extracted, point dipole polarizability," J. Appl. Phys. **115**, 024306 (2014).

64. G. T. Forcherio, P. Blake, D. DeJarnette, and D. K. Roper, "Nanoring structure, spacing, and local dielectric sensitivity for plasmonic resonances in square lattices," Opt. Express. *Submitted April, 2014*.

65. J. Aizpurua, P. Hanarp, D. Sutherland, M. Käll, G. Bryant, and F. J. García de Abajo, "Optical properties of gold nanorings," Phys. Rev. Lett. **90**, 057401 (2003).

66. C.-Y. Tsai, S.-P. Lu, J.-W. Lin, and P.-T. Lee, "High sensitivity plasmonic index sensor using slablike gold nanoring arrays," Appl. Phys. Lett. **98**, 153108 (2011).

67. C.-Y. Tsai, J.-W. Lin, C.-Y. Wu, P.-T. Lin, T.-W. Lu, and P.-T. Lee, "Plasmonic coupling in gold nanoring dimers: observation of coupled bonding mode," Nano Lett. **12**, 1648–1654 (2012).

68. J. Ye, P. Van Dorpe, L. Lagae, G. Maes, and G. Borghs, "Observation of plasmonic dipolar anti-bonding mode in silver nanoring structures," Nanotechnology **20**, 465203 (2009).

69. F. Hao, E. M. Larsson, T. A. Ali, D. S. Sutherland, and P. Nordlander, "Shedding light on dark plasmons in gold nanorings," Chem. Phys. Lett. **458**, 262–266 (2008).

70. H.-Y. Tseng, C.-K. Lee, S.-Y. Wu, T.-T. Chi, K.-M. Yang, J.-Y. Wang, Y.-W. Kiang, C. C. Yang, M.-T. Tsai, Y.-C. Wu, H.-Y. E. Chou, and C.-P. Chiang, "Au nanorings for enhancing absorption and backscattering monitored with optical coherence tomography," Nanotechnology **21**, 295102 (2010).

71. C. Huang, J. Ye, S. Wang, T. Stakenborg, and L. Lagae, "Gold nanoring as a sensitive plasmonic biosensor for on-chip DNA detection," Appl. Phys. Lett. **100**, 173114 (2012).

72. J. Aizpurua, L. Blanco, P. Hanarp, D. S. Sutherland, M. Käll, G. W. Bryant, and F. J. García de Abajo, "Light scattering in gold nanorings," J. Quant. Spectrosc. Radiat. Transf. **89**, 11–16 (2004).

73. G. Mie, "Beiträge zur Optik trüber Medien, speziell kolloidaler Metallösungen," Ann. Phys. **330**, 377–445 (1908).

74. T. W. Ebbesen, H. J. Lezec, H. F. Ghaemi, T. Thio, and P. A. Wolff, "Extraordinary optical transmission through sub-wavelength hole arrays," Nature **391**, 667–669 (1998).

75. H. Ghaemi, T. Thio, D. Grupp, T. Ebbesen, and H. Lezec, "Surface plasmons enhance optical transmission through subwavelength holes," Phys. Rev. B **58**, 6779–6782 (1998).

76. H. Bethe, "Theory of diffraction by small holes," Phys. Rev. **66**, 163–182 (1944).

77. A. Degiron and T. W. Ebbesen, "The role of localized surface plasmon modes in the enhanced transmission of periodic subwavelength apertures," J. Opt. A **7**, S90–S96 (2005).

78. C. Genet and T. W. Ebbesen, "Light in tiny holes," Nature **445**, 39–46 (2007).

79. R. Gordon, D. Sinton, K. L. Kavanagh, and A. G. Brolo, "A new generation of sensors based on extraordinary optical transmission," Acc. Chem. Res. **41**, 1049–1057 (2008).

80. T. Thio, H. F. Ghaemi, H. J. Lezec, P. A. Wolff, and T. W. Ebbesen, "Surface-plasmon-enhanced transmission through hole arrays in Cr films," J. Opt. Soc. Am. B **16**, 1743–1748 (1999).

81. H. J. Lezec and T. Thio, "Diffracted evanescent wave model for enhanced and suppressed optical transmission through subwavelength hole arrays," Opt. Express **12**, 3629–3651 (2004).

82. H. Gao, J. Henzie, and T. W. Odom, "Direct evidence for surface plasmon-mediated enhanced light transmission through metallic nanohole arrays.," Nano Lett. **6**, 2104–2108 (2006).

83. M. Babinet, "Babinet, M.," C. R. Acad. Sci. **4**, 638 (1837).

84. T. Zentgraf, T. Meyrath, A. Seidel, S. Kaiser, H. Giessen, C. Rockstuhl, and F. Lederer, "Babinet's principle for optical frequency metamaterials and nanoantennas," Phys. Rev. B **76**, 033407 (2007).

85. J. D. Edmunds, M. C. Taylor, A. P. Hibbins, J. R. Sambles, and I. J. Youngs, "Babinet's principle and the band structure of surface waves on patterned metal arrays," J. Appl. Phys. **107**, 103108 (2010).

86. M. Hentschel, T. Weiss, S. Bagheri, and H. Giessen, "Babinet to the half: coupling of solid and inverse plasmonic structures," Nano Lett. **13**, 4428–4433 (2013).

87. D. Rossouw and G. A. Botton, "Resonant optical excitations in complementary plasmonic nanostructures," Opt. Express **20**, 6968–6973 (2012).

88. C. M. Watts, X. Liu, and W. J. Padilla, "Metamaterial electromagnetic wave absorbers," Adv. Mater. **24**, OP98–120, OP181 (2012).

89. P. Franken, A. Hill, C. Peters, and G. Weinreich, "Generation of optical harmonics," Phys. Rev. Lett. **7**, 118–119 (1961).

90. N. Bloembergen and P. Pershan, "Light waves at the boundary of nonlinear media," Phys. Rev. **128**, 606–622 (1962).

91. S. A. Maier and H. A. Atwater, "Plasmonics: Localization and guiding of electromagnetic energy in metal/dielectric structures," J. Appl. Phys. **98**, 011101 (2005).

92. A. Capretti, G. F. Walsh, S. Minissale, J. Trevino, C. Forestiere, G. Miano, and L. Dal Negro, "Multipolar second harmonic generation from planar arrays of Au nanoparticles," Opt. Express **20**, 15797–15806 (2012).

93. G. F. Walsh and L. Dal Negro, "Enhanced second harmonic generation from Au nanoparticle arrays by femtosecond laser irradiation," Nanoscale **5**, 7795–7799 (2013).

94. M. McMahon, R. Lopez, R. Haglund, E. Ray, and P. Bunton, "Second-harmonic generation from arrays of symmetric gold nanoparticles," Phys. Rev. B **73**, 041401 (2006).

95. M. D. McMahon, D. Ferrara, C. T. Bowie, R. Lopez, and R. F. Haglund Jr., "Second harmonic generation from resonantly excited arrays of gold nanoparticles," Appl. Phys. B **87**, 259–265 (2007).

96. S. Kujala, B. K. Canfield, M. Kauranen, Y. Svirko, and J. Turunen, "Multipolar analysis of second-harmonic radiation from gold nanoparticles," Opt. Express **16**, 17196–17208 (2008).

97. J. Nappa, G. Revillod, I. Russier-Antoine, E. Benichou, C. Jonin, and P. Brevet, "Electric dipole origin of the second harmonic generation of small metallic particles," Phys. Rev. B **71**, 165407 (2005).

98. D. DeJarnette, J. Norman, and D. K. Roper, "Attribution of Fano resonant features to plasmonic particle size, lattice constant, and dielectric wavenumber in square nanoparticle lattices," Photonics Res. **2**, 15–23 (2014).

99. G. F. Walsh and L. D. Negro, "Engineering plasmon-enhanced Au light emission with planar arrays of nanoparticles," Nano Lett. **13**, 786–792 (2013).

100. J. Butet, J. Duboisset, G. Bachelier, I. Russier-Antoine, E. Benichou, C. Jonin, and P.-F. Brevet, "Optical second harmonic generation of single metallic nanoparticles embedded in a homogeneous medium," Nano Lett. **10**, 1717–1721 (2010).

101. A. Boltasseva and V. M. Shalaev, "Fabrication of optical negative-index metamaterials: recent advances and outlook," Metamaterials **2**, 1–17 (2008).

102. D. S. Ginger, H. Zhang, and C. A. Mirkin, "The evolution of dip-pen nanolithography," Angew. Chemie **43**, 30–45 (2004).

103. C. Vieu, F. Carcenac, A. Pépin, Y. Chen, M. Mejias, A. Lebib, L. Manin-Ferlazzo, L. Couraud, and H. Launois, "Electron beam lithography: resolution limits and applications," Appl. Surf. Sci. **164**, 111–117 (2000).

104. S. Cabrini, A. Carpentiero, R. Kumar, L. Businaro, P. Candeloro, M. Prasciolu, A. Gosparini, C. Andreani, M. De Vittorio, T. Stomeo, and E. Di Fabrizio, "Focused ion beam lithography for two dimensional array structures for photonic applications," Microelectron. Eng. **78-79**, 11–15 (2005).

105. S. Y. Chou, P. R. Krauss, and P. J. Renstrom, "Nanoimprint lithography," J. Vac. Sci. Technol. B **14**, 4129–4133 (1996).

106. C. L. Haynes and R. P. Van Duyne, "Nanosphere lithography: a versatile nanofabrication tool for studies of size-dependent nanoparticle optics," J. Phys. Chem. B **105**, 5599–5611 (2001).

107. F. J. García de Abajo, "Optical excitations in electron microscopy," Rev. Mod. Phys. **82**, 209–275 (2010).

108. P. Blake, W. Ahn, and D. K. Roper, "Enhanced uniformity in arrays of electroless plated spherical gold nanoparticles using tin presensitization," Langmuir **26**, 1533–1538 (2010).

109. J. J. Dumond and H. Yee Low, "Recent developments and design challenges in continuous roller micro- and nanoimprinting," J. Vac. Sci. Technol. B **30**, 010801 (2012).

110. P. Blake, S. Kühne, G. T. Forcherio, and D. K. Roper, "Diffraction in nanoparticle lattices increases sensitivity of localized surface plasmon resonance to refractive index changes," J. Nanophotonics. *Accepted April 9th, 2014*.

111. W. Kubo and S. Fujikawa, "Au double nanopillars with nanogap for plasmonic sensor," Nano Lett. **11**, 8–15 (2011).

112. S. Kim, J.-M. Jung, D.-G. Choi, H.-T. Jung, and S.-M. Yang, "Patterned arrays of Au rings for localized surface plasmon resonance," Langmuir **22**, 7109–7112 (2006).

113. B. Radha, S. H. Lim, M. S. M. Saifullah, and G. U. Kulkarni, "Metal hierarchical patterning by direct nanoimprint lithography," Sci. Rep. **3**, 1078 (2013).

114. L. Jiao, H. Gao, G. Zhang, G. Xie, X. Zhou, Y. Zhang, Y. Zhang, B. Gao, G. Luo, Z. Wu, T. Zhu, J. Zhang, Z. Liu, S. Mu, H. Yang, and C. Gu, "Fabrication of metallic nanostructures by negative nanoimprint lithography," Nanotechnology **16**, 2779–2784 (2005).

115. G. T. Forcherio, J. R. Dunklin, J. Proctor, and D. K. Roper, "Deposition of periodic plasmonic structures onto poly(dimethylsiloxane) via interfacial reduction of noble-metal salts." *In Preparation*.

116. M. Knoll and E. Ruska, "Das elektronenmikroskop," Zeitschrift für Phys. **78**, 318–339 (1932).

117. S. M. Lindsay, *Introduction to Nanoscience* (Oxford University Press, 2010).

118. R. F. Egerton, "Electron energy-loss spectroscopy in the TEM," Reports Prog. Phys. **72**, 016502 (2009).

119. J. Nelayah, M. Kociak, O. Stéphan, F. J. García de Abajo, M. Tencé, L. Henrard, D. Taverna, I. Pastoriza-Santos, L. M. Liz-Marzán, and C. Colliex, "Mapping surface plasmons on a single metallic nanoparticle," Nat. Phys. **3**, 348–353 (2007).

120. A. Hörl, A. Trügler, and U. Hohenester, "Tomography of particle plasmon fields from electron energy loss spectroscopy," Phys. Rev. Lett. **111**, 076801 (2013).

121. C. Powell and J. Swan, "Origin of the characteristic electron energy losses in aluminum," Phys. Rev. **115**, 869–875 (1959).

122. N. Geuquet and L. Henrard, "EELS and optical response of a noble metal nanoparticle in the frame of a discrete dipole approximation," Ultramicroscopy **110**, 1075–1080 (2010).

123. J. Z. Zhang, *Optical Properties and Spectroscopy of Nanomaterials* (World Scientific Publishing Co., 2009), p. 209.

124. H. Kuzmany, *Solid-State Spectroscopy*, 2nd ed. (Springer, 2010).

125. E. Hecht, *Optics*, 4th ed. (Addison-Wesley, 2001).

126. D. Kim, S. Hohng, V. Malyarchuk, Y. Yoon, Y. Ahn, K. Yee, J. Park, J. Kim, Q. Park, and C. Lienau, "Microscopic origin of surface-plasmon radiation in plasmonic band-gap nanostructures," Phys. Rev. Lett. **91**, 143901 (2003).

127. G. T. Forcherio and D. K. Roper, "Optical attenuation of plasmonic nanocomposites within photonic devices," Appl. Opt. **52**, 6417–6427 (2013).

128. J. R. Dunklin, G. T. Forcherio, K. R. Berry, and D. K. Roper, "Gold nanoparticle–polydimethylsiloxane thin films enhance thermoplasmonic dissipation by internal reflection," J. Phys. Chem. C **118**, 7523-7531 (2014).

129. G. Bachelier, J. Butet, I. Russier-Antoine, C. Jonin, E. Benichou, and P.-F. Brevet, "Origin of optical second-harmonic generation in spherical gold nanoparticles: Local surface and nonlocal bulk contributions," Phys. Rev. B **82**, 235403 (2010).

130. M. L. Sandrock, C. D. Pibel, F. M. Geiger, and C. A. Foss, "Synthesis and second-harmonic generation studies of noncentrosymmetric gold nanostructures," J. Phys. Chem. B **103**, 2668–2673 (1999).

131. M. Lisunova, X. Wei, D. DeJarnette, G. T. Forcherio, K. Berry, P. Blake, and D. K. Roper, "Photothermal response of the plasmonic nanoconglomerates in assembled films by electroless plating approach," Energy Environ. Sci. *Submitted January, 2014*.

APPENDIX

A: Description of Research for Popular Publication

The global strive to run on "green" power has served as a motivational cornerstone for scientific research and innovation over the last two decades. Much of this research has focused on developing more efficient ways to create energy, such as solar cells, or ways to store and transport energy, such as battery technology. These areas have seen a high degree of success, and the technologies previously seen as improbable, have become a market reality. Gregory T. Forcherio, a Masters student in MicroElectronics-Photonics at the University of Arkansas asks, "But what happens half a century from now, as global energy demands will continue to rise with an ever-climbing population? Will there be enough supply to meet demands, considering fossil fuels and availability of fissile Uranium are past their peak?"

Forcherio and his advisor, Dr. D. Keith Roper, envision recycling heat energy. Approximately 60% of energy generated in the world is wasted as dissipated heat. As this heat is given away, either by skin, a car engine, or a computer processor, it appears that it may be converted into electrical or optical energy using nanoparticles. Forcherio and Roper have worked on a class of metamaterials (artificial materials comprised of nano-sized, metal particulates) which would allow thermal energy to be absorbed and re-emitted as visible light according to the size, shape, and arrangement of gold particles. This "converted" optical emission could be used as a stand-alone signal, or even transformed into electricity using semiconductors.

Recovering even a fraction of the world's wasted thermal energy could reduce global energy demands, and create opportunities for new types of devices. "Imagine medical devices tailored for in-field monitoring of soldiers powered by personal energy networks based on

dissipated body heat," Forcherio exclaims excitedly. Amazingly, such a device could be hosted within a polymer film less than the thickness of a few human hairs. Similarly, these emissive metamaterials could finally provide a feasible platform for integrating high-speed optical circuits into pre-existing electronic devices by harvesting their heat, which has been a key barrier in increasing processor clock speeds. These represent only a few examples this untapped energy source could bring into technological reality.

But how could such a particular metamaterial be made on a large enough scale to provide any amount of useable power? Current processes for making metamaterials require large, specialized, expensive equipment under energy-intensive, extreme environments not intended for high-volume manufacturing. Forcherio and colleagues Jeremy Dunklin and James Proctor are developing a new method for creating nanoparticles in polymer films under room ambient conditions without the need of any special equipment. "One could make these metamaterials in their kitchen overnight with this process," explains Dunklin. After the conditions and process are optimized, Forcherio and Roper believe this process represents a major breakthrough of bringing nano-research into the technology marketplace.

B: Executive Summary of Newly Created Intellectual Property

The following list indicates newly created intellectual items.

1. Design and construction of bi-directional spectroscopic apparatus built around an integrating sphere for the measurement of far-field transmission, reflection, and attenuation for a planar media.
2. Rapid modeling technique of using polarizability extraction between approximate dipole algorithms to evaluate the spectral response of two dimensional lattices of arbitrarily shaped nanostructures.

C: Potential Patent and Commercialization Aspects of Intellectual Property Items

C.1 Patentability of Intellectual Property

Potential patentability of each item in Appendix B was considered. It was determined that the items could be patented. This is described in detail for each item below:

1. The bi-directional spectroscopy apparatus was assembled from commercially available parts, modules, and computer software. The schematic and text description of the apparatus has been published by the Optical Society of America on September 1st, 2013 (Forcherio *et al.* Appl. Opt. (2013)). This item is patentable for 4 months. However, it is the opinion of the author that a patent should not be pursued. Apparatuses exist which use similar combinations of components, so the patent could be circumvented.
2. The polarizability extraction modeling technique extends the use of rapid dipole approximation algorithms established in the literature for spheroids to arbitrary structures. The approach was described in full for publication by the American Institute of Physics on January 10th, 2014 (DeJarnette *et al.* J. Appl. Phys. (2014)). This item is patentable for 7 months. It is the opinion of the author that this modeling technique does not warrant pursuit of a patent, as it is a variation on established modeling techniques.

C.2 Commercialization Aspects

The commercialization opportunities of each item in Appendix B were considered. Among them, none of them have commercial appeal. These considerations are described in detail for each item below:

1. The bi-directional spectroscopy apparatus is commercially viable as a research tool. This would require optimization of the materials and components used. However similar apparatuses could be built for the unique purposes of a particular research organization.

The adaptability of this, and similar, apparatuses to comprehensively measure optical interactions in planar samples would be of interest to the scientific research community, but a patent could be circumvented by non-licensing organizations.

2. The polarizability extraction modeling technique does not exhibit commercial appeal. The technique was tested and put into practice using freeware. A bridged software package between the two distinct model algorithms using this technique could be of interest to a subset of the scientific research community, but poses additional barriers which are circumvented by the ease of its current implementation.

C.3 Possible Prior Disclosure of Intellectual Property

1. The schematic and description of the bi-directional spectroscopy apparatus was published by me as the lead author on September 1st, 2013 (Forcherio *et al.* Appl. Opt. (2013)). C. Chambers and C. Bodinger featured a schematic and description of this apparatus in a report and April 19th, 2014 presentation for the requirements of the Freshman Engineering Program.
2. The polarizability extraction modeling technique was published by D. DeJarnette with me as a co-author on January 10th, 2014 (DeJarnette *et al.* J. Appl. Phys. (2014)).

D: Broader Impact of Research

D.1 Applicability of Research Methods to Other Problems

The concepts discussed in this thesis can be applied to other novel opto-electronic devices. Ordering plasmonic nanoparticles onto/into polymeric thin-films could be of interest in plasmon-enhanced organic photovoltaic cells, DNA melting analysis, lab-on-a-chip biological sensing, biofuel separations, and flexible optical circuitry. For example, introducing nanoparticles into microfluidic channels of a PDMS chip could result in a low-cost, portable sensory apparatus that could be used for label-free biological analyte detection.

D.2 Impact of Research Results on U.S. and Global Society

Optically visible emission from thermally stimulated metamaterials could ultimately enable the recovery of waste heat, which constitutes 60% of generated energy around the world. For example, thermophotovoltaic devices could harvest heat by using an emissive metamaterial as a photon source. This work could develop metamaterials that convert heat dissipated from conventional silicon devices into high-speed visible optical signals, providing a platform for photonic circuitry. Lab-on-a-chip medical monitoring could be powered with personal power networks based on harvested body heat from flexible metamaterials integrated into clothing. These are three initial examples of thermal energy harvesting that could reduce global demand for power generation and consumption, and open up opportunities for new devices.

D.3 Impact of Research Results on the Environment

Thermal energy harvesting would reduce the demand of power generation due to energy recycling, thus eliminating a portion of green-house gas emission. Effects deemed detrimental to the environment from nanoparticles escaping their host matrix have yet to be reported.

E: Microsoft Project for M.S. MicroEP Degree Plan

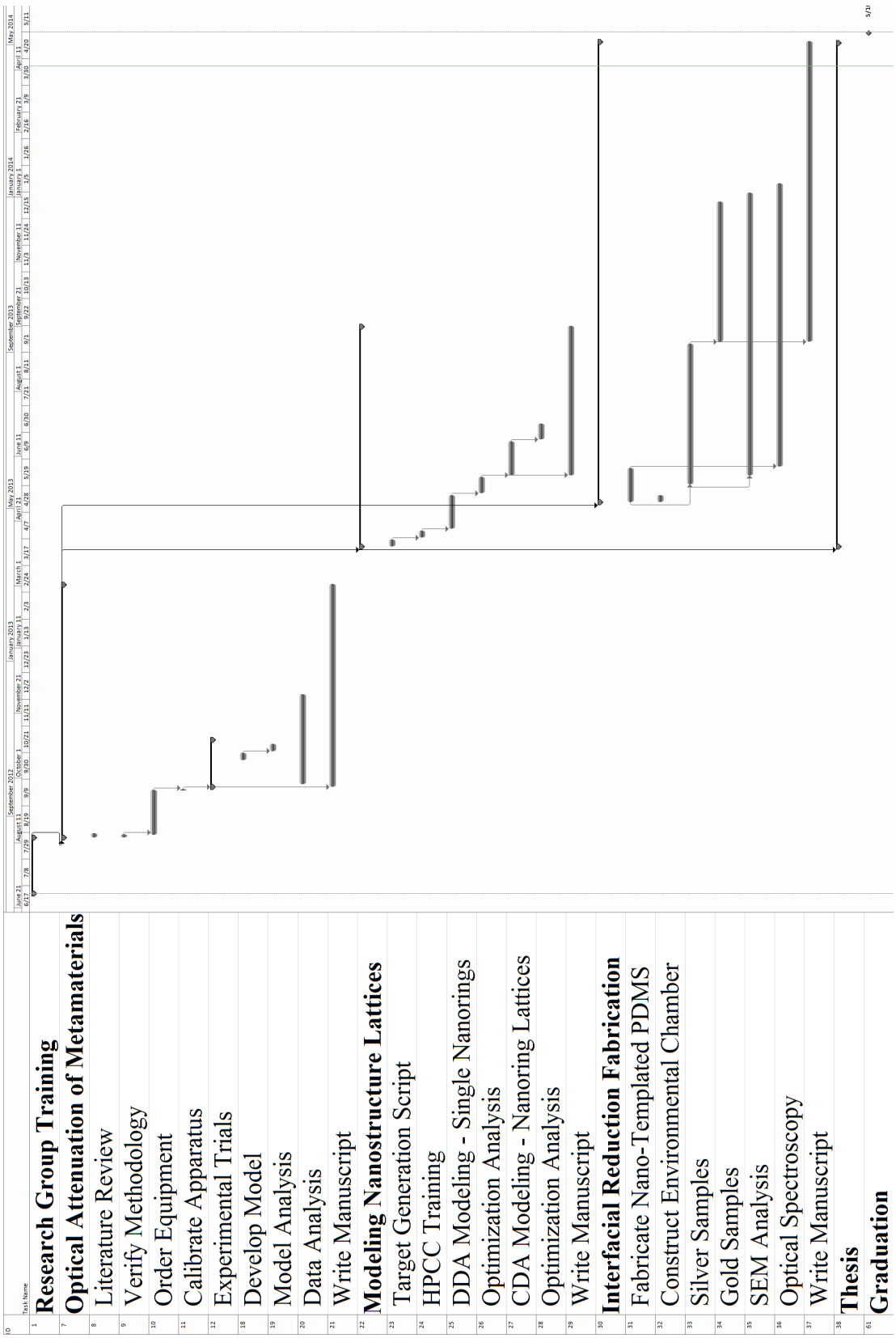

F: Identification of All Software Used in Research and Thesis Generation

Computer #1:
- Model: Dell Precision T3500
- Serial Number: DCRB3L1
- Location: Institute for Nanoscience and Engineering, Room 301
- Owner: NanoBio Photonics Lab, University of Arkansas

Software #1:
- Name: Microsoft Office, Professional 2010
- Purchased By: Department of Chemical Engineering, University of Arkansas
- License: 02260-018-0000106-48503

Software #2:
- Name: Mendeley (v. 1.9.2)
- Purchased By: Gregory T. Forcherio
- License: Freeware

Software #3:
- Name: Matlab R2012a (v. 7.14)
- Purchased By: Department of Chemical Engineering, University of Arkansas
- License: 601103

Computer #2:
- Model: Dell Optiplex 755
- Serial Number: 405SHH1
- Location: Institute for Nanoscience and Engineering, Room 251
- Owner: NanoBio Photonics Lab, University of Arkansas

Software #1:
- Name: AvaSoft 7.7
- Purchased By: NanoBio Photonics Lab, University of Arkansas
- License: Freeware

Computer #3:
- Model: ASUS VivoBook X202E
- Serial Number: D2N0BC006118059
- Location: Home
- Owner: Gregory T. Forcherio

Software #1:
- Name: Microsoft Office, Student 2013
- Purchased By: Gregory T. Forcherio
- License: 00201-10029-87936-AA358

G: All Publications Published, Submitted, and Planned

Publications Published

- G.T. Forcherio and D.K. Roper, "Optical attenuation of plasmonic nanocomposites within photonic devices," Appl. Opt. **52**, 6417-6427 (2013).
- J.R. Dunklin, G.T. Forcherio, K.R. Berry, and D.K. Roper, "Asymmetric reduction of gold nanoparticles into thermoplasmonic polydimethylsiloxane thin films," ACS Appl. Mater. Interfaces **5**, 8457-8466 (2013).
- M. Lisunova, J.C. Norman, P. Blake, G.T. Forcherio, D.F. DeJarnette, D.K. Roper, "Modulation of plasmonic Fano resonance by the shape of the nanoparticles in ordered arrays," J. Phys. D: Appl. Phys. **46**, 485103 (2013).
- D. DeJarnette, P. Blake, G.T. Forcherio, and D.K. Roper, "Far-field Fano resonance in nanoring lattices modeled from extracted, point dipole polarizability," J. Appl. Phys. **115**, 024306 (2014).
- J.R. Dunklin, G.T. Forcherio, and D.K. Roper, "Geometric optics of gold nanoparticle-polydimethylsiloxane thin film systems," Opt. Mater. Express **4**, 375-383 (2014).
- J.R. Dunklin, G.T. Forcherio, K.R. Berry, D.K. Roper, "Gold nanoparticle-polydimethylsiloxane thin films enhance thermoplasmonic heating by internal reflection," J. Phys. Chem. **118**, 7523-7531.
- P. Blake, S. Kühne, G.T. Forcherio, and D.K. Roper, "Diffraction in nanoparticle lattices increases sensitivity of localized surface plasmon resonance to refractive index changes," J. Nanophotonics. Accepted April 2014.

Publications Submitted

- G.T. Forcherio, P. Blake, D. DeJarnette, and D.K. Roper, "Nanoring structure, spacing, and local dielectric sensitivity for plasmonic resonances in square lattices," Opt. Express.
- M. Lisunova, X. Wei, D. DeJarnette, G.T. Forcherio, K.R. Berry, P. Blake, D.K. Roper, "Photothermal response of the plasmonic nanoconglomerates in assembled films by electroless plating approach," Energy Environ. Sci.

Publications Planned

- G.T. Forcherio, J.R. Dunklin, J. Proctor, and D.K. Roper, "Deposition of periodic plasmonic structures onto poly(dimethylsiloxane) via interfacial reduction of noble-metal salts."